



# LIMA (v2.0): A full two-moment cloud microphysical scheme for the mesoscale non-hydrostatic model Meso-NH v5-6

Marie Taufour<sup>1</sup>, Jean-Pierre Pinty<sup>1</sup>, Christelle Barthe<sup>1</sup>, Benoît Vié<sup>2</sup>, and Chien Wang<sup>1</sup>

<sup>1</sup>Laboratoire d'Aérologie, Université de Toulouse, UT3, CNRS, IRD, Toulouse, France

<sup>2</sup>Centre National de Recherches Météorologiques - UMR 3589, Toulouse, France

**Correspondence:** Christelle Barthe ([christelle.barthe@cnrs.fr](mailto:christelle.barthe@cnrs.fr))

**Abstract.** A full two-moment microphysics parameterisation of the LIMA scheme (hereafter named LIMA v2.0) has been developed and successfully implemented in the Meso-NH cloud-resolving model. The novelty of the scheme is a set of prognostic equations of the number concentration of each precipitating ice category (snow-aggregates, graupel and hail), in complement to the prediction of the mass mixing ratios. As a result, new microphysical conversion rates are introduced and explicitly computed using the size distributions of the hydrometeors.

The new LIMA v2.0 scheme has been tested for an idealized deep convection case against the original LIMA scheme characterized by an empirical number concentration-mixing ratio relationship applied to the precipitating ice. Inclusion of number concentration equations for the snow-aggregates and graupel significantly alters the microphysical structure and dynamical evolution of the simulated supercell. When comparing to the results obtained with the previous version of LIMA, the new v2.0 of the scheme tends to increase the pristine ice mixing ratio, to decrease the other ice hydrometeors, and to enhance the feedbacks between raindrops and the ice phase. The new scheme is also more efficient to produce earlier raindrops at ground level and to reduce hail precipitation.

## 1 Introduction

Cloud microphysical processes play a central role in determining the life cycle of the clouds, the formation of precipitation as well as the radiative transfer in cloudy environment. The response of these processes to the variation of aerosol fields under different dynamical and thermodynamical backgrounds is also essential in estimating the impacts of natural and anthropogenic aerosols on Earth's radiative budget, water cycle, and atmospheric circulation as well as weather patterns (e.g., Lau et al., 2006; Christensen and Stephens, 2011; van den Heever et al., 2011; Tao et al., 2012; Goren and Rosenfeld, 2012; Lee, 2012). An adequate representation of cloud microphysical processes in climate and weather models is thus essential for high quality projections.

Laboratory studies (e.g., Simpson, 1983; Schnaiter et al., 2016; Simpson et al., 2018) alongside real-world case studies (e.g., Heymsfield et al., 2002, 2010, 2013; Delanoë et al., 2005, 2014) have long sustained the advancements of knowledge that benefit to the development of many microphysical schemes. However, these developments still lack of consensus due to the fact that some microphysical features can be described with more or less sophistication in the limit of the computational



25 resources. In addition, uncertainties also remain in the current numerical schemes particularly those concerning ice phase processes (McFarquhar et al., 2017).

Current microphysics schemes can be categorized into two major types: i.e., the bin schemes (e.g., Hall, 1980; Khain et al., 2000) characterized by discretized size distributions with tens of state prognostic variables, and the modal schemes (e.g., Walko et al., 1995; Pinty and Jabouille, 1998; Thompson et al., 2004), where only one, two or even three moments of the particle size  
30 distributions (PSD) are deemed to be sufficient to describe the microphysics states. Owing to their computational efficiency, the moment schemes with different degrees of complexity have been mostly used in a vast majority of applications with a focus on cloud dynamics or microphysics-dynamics interactions. For example, Straka and Mansell (2005) developed a single-moment bulk scheme using mass as the sole prognostic variable, subdividing icy hydrometeors into ten categories according to their shape, size and density, including columnar or wafer-shaped ice crystals, frozen cloud water droplets, snow, three categories for  
35 graupel of different densities, frozen drops, and two types for graupel separated by their size. This type of scheme for ice phase processes is an attempt to improve the representation of the variety of convective systems by limiting the assumptions made during derivation of parameterizations. Nevertheless, Srivastava (1978) highlighted the advantages of adopting two prognostic moments in determining the PSD of hydrometeors in modeling microphysical processes. Two-moment microphysical schemes have then been developed, allowing more degrees of freedom and thus a better representation of the complex microphysical  
40 processes. In such schemes, the number concentration alongside the mixing ratio are commonly selected as the two prognostic moments. Early works chose to represent only one species with 2-moment method, for example the cloud water (Nickerson et al., 1986) or the primary ice crystals (Cotton et al., 1986), while others developed a 2-moment representation for only a part of the hydrometeors, leaving the rest for single moment representation (e.g., Ziegler, 1985; Ferrier, 1994; Vié et al., 2016). This strategy perhaps also reflects an attempt to balance between the need of an excessively complicated cloud microphysics  
45 schemes and the need for extra parameters such as the role of aerosol in modeling cloud microphysics and evolution. The first full 2 moment schemes (Murakami, 1990; Wang and Chang, 1993; Meyers et al., 1997) were developed to allow a more realistic representation of the cloud systems when compared to radar observations. Subsequently, microphysical parameterizations with 2 or even more moments have become more popular (Reisner et al., 1998; Cohard and Pinty, 2000a; Khairoutdinov and Kogan, 2000; Seifert and Beheng, 2006b; Morrison et al., 2009, and many others) and 2 moment schemes are part of the state  
50 of the art in cloud modeling at high resolution.

In recent years, numerous studies have demonstrated the contribution of multi-momentum parametrisations in making significant improvement of models' performance. Good examples include the better parameterised processes such as sedimentation (taking into account size sorting, Milbrandt and Yau, 2006; Dawson et al., 2010), or evaporation processes with feedback to  
55 updrafts or cold zones under systems (Seifert and Beheng, 2006a; Morrison et al., 2009; Noppel et al., 2010). Comparisons of these studies with available observations are also greatly improved by the addition of precision in estimating of dispersive parameters such as hydrometeor sizes or reflectivities. Seifert et al. (2006) have shown that for an idealised supercell case, the results with a 2-moment scheme are similar to those obtained with a bin-type parameterisation. Nevertheless, these multi-moment diagrams also require the developers to check more carefully the shape parameters (related to the fall speed or the



60 density of the hydrometeors) or the impact of the different parameterisations chosen by the developers on the results. Indeed, the conclusions on the impact of aerosol populations or on simulated total precipitation vary according to the type of system (Seifert and Beheng, 2006a), but are also strongly influenced by the different schemes, more than by the addition of moments to describe the hydrometeors in the same scheme (Milbrandt et al., 2010).

The development of a fully 2 moment microphysics scheme still raises the concern of the real benefit to include a set of prognostic equations for each icy hydrometeor concentration. It is very likely that the task itself is not straightforward due to the non-linearity of the microphysics processes. For instance, a difficulty is to set the proper boundaries of the graupel PSD for integration over the particle sizes. More importantly, a true difficulty is to provide a robust and consistent parameterization of the fundamental conversion processes that transfer both mixing ratio and number concentration from one category of ice hydrometeor to the other one. The snow-aggregate particle case is probably the easiest case to treat because it is similar to that of the raindrops which are generated by the autoconversion (coalescence) of the cloud droplets. According to Harrington et al. (1995), an estimate of 150 microns is an acceptable size limit between the pristine ice crystals and the snow-aggregate category. This value corresponds more or less to the size that small ice crystals should grow by water vapor deposition before experiencing riming by the cloud droplets or ice crystal self-aggregation (Pruppacher and Klett, 1997). The onset of pristine ice riming depends on the crystal habit but the mean size of 150 microns seems to well cover most of the cases (Wang and Ji, 2000). So the growth-conversion scheme of Harrington et al. (1995) can be fully applied to calculate the rates of both mass mixing ratio and number concentration to feed the snow-aggregate particles. In contrast, there are two generating sources of graupel particles in the LIMA scheme: the raindrop freezing after contact with a small ice crystal and the intense riming of the snow-aggregate hydrometeors. In the first case, a tendency of the graupel number concentration can be computed because number concentrations of the raindrops and pristine ice crystals are locally available. Conversely, the expression of a number concentration tendency for the riming-conversion process of the aggregates depends on the way "light" and "heavy" riming intensities are formally defined. All these questions are examined in the next section.

This work describes a full 2 moment microphysical scheme for mixed phase clouds developed for the non-hydrostatic mesoscale model Meso-NH (Lafore et al., 1998; Lac et al., 2018). The original microphysics scheme, the Liquid, Ice, Multiple Aerosols (LIMA) module (Vié et al., 2016) is partially based on a 2-moment representation of the liquid-phase hydrometeors following the original warm microphysics scheme of Cohard and Pinty (2000a). In this study, a full 2 moment version of the original LIMA v1.0 scheme (Vié et al., 2016) has been developed. It is thereby able to describe cloud, rain and all ice hydrometeors using two moments of the size distribution, allowing a better consistency in the treatment of the physical processes, in particular those related to ice phase processes (Vié et al., 2016; Hoarau et al., 2018a). The new version of the LIMA scheme, hereinafter referred to as LIMA v2.0, is described in the first section of the paper, with a focus on the treatment of the snow-aggregate and graupel number concentration tendencies. The second section is dedicated to the different behaviors of the two versions of LIMA in simulating the same idealized supercell case. Finally a conclusion is drawn on the specific properties of the full 2 moment microphysics scheme LIMA, in particular the advantage to reinforce the decoupling between mixing ratios and number concentrations to offer more flexibility to the simulation of cloud evolution.



## 2 Model description

### 95 2.1 Short overview of Meso-NH

The regional scale model Meso-NH (Mesoscale Non-Hydrostatic, Lafore et al., 1998; Lac et al., 2018) was initially jointly developed by Laboratoire d'Aérodynamique and Centre National de Recherches Météorologiques in Toulouse (France). A detailed description of the successive versions of the code is available in the scientific documentation of the model (<http://mesonh.aero.obs-mip.fr>). Meso-NH is a high resolution limited area research model for the simulation of idealized cases (selected cases to study certain aspects of the modeled subject) or the simulation of real meteorological situations over complex terrain with initialization and coupling data analyses derived from models. Many subgrid scale physical parameterizations are available in the package, such as an EXternalized SURFace submodel (SURFEX, Masson et al., 2013) including a dynamical ocean-wave coupling (Voldoire et al., 2017; Pianezze et al., 2018), deep and shallow convective mass-flux and turbulent schemes (Cuxart et al., 2000; Bechtold et al., 2001; Pergaud et al., 2009), and several microphysics schemes (Cohard and Pinty, 2000a; Vié et al., 2016) coupled to a standard radiative transfer scheme (Morcrette, 1991; Mlawer et al., 1997) and more recently to the radiation scheme of the ECMWF model (ecRad, Hogan and Bozzo, 2018).

### 2.2 Summary of the LIMA microphysical scheme

The scheme described in this paper is an extension of the previous LIMA v1.0 microphysics scheme (Liquid, Ice, Multiple Aerosols, Vié et al., 2016). LIMA v1.0 is partially 2-moment with a primary focus on the representation of aerosol-cloud interactions. In detail, LIMA has a 2 moment representation only for the liquid-phase hydrometeors (cloud droplets and rain drops) and for the primary ice crystals. The whole population of aerosols is categorized into CCN (Cloud Condensation Nuclei) and IFN (Ice Freezing Nuclei) which can form primary droplets and pristine ice crystals, via activation or/and nucleation respectively. LIMA is sensitive to the competition among lognormal PSD parameters and composition of the CCN, and to the lognormal PSD characteristics and solubility of the IFN, as well.

115 LIMA v1.0 predicts the mass mixing ratio  $r$  (the mass of water scaled by the reference mass of dry air  $\rho_a$ ) of six water species: water vapour, cloud water, rain water, primary ice crystals, snow/aggregates and graupel, and number concentration ( $N$ ) for cloud water, rain water, and ice crystals. Hail is an optional category of hydrometeors depending on the dry/wet growth modes of the graupel.

The PSD for each hydrometeor follows a generalized Gamma distribution:

$$120 \quad n(D) = N \frac{\alpha}{\Gamma(\nu)} (\lambda D)^{\alpha\nu} D^{-1} e^{-(\lambda D)^\alpha}, \quad (1)$$

where  $D$  is the diameter of the particle,  $\alpha$  and  $\nu$  are free shape parameters (see Table 1 for their values), and  $\Gamma(\cdot)$  the Gamma function. For snow, graupel and hail the number concentration  $N$  is estimated following the relation:  $N = C\lambda^x$  (where  $C$  and  $x$  are fixed parameters in Table 1). The slope parameter  $\lambda$  is a function of the number concentration and the mixing ratio,

$$\lambda = \left( a \frac{N}{r} \frac{\Gamma(\nu + b/a)}{\Gamma(\nu)} \right)^{\frac{1}{b}}. \quad (2)$$



125 using a mass-size relationship  $m(D) = aD^b$  for the liquid and ice condensate, with  $a$  and  $b$  fixed parameters described in Table 1. The terminal fall velocity  $v(D)$  is also related to the particle size  $D$  (equivalent to the diameter for the drops):

$$v(D) = cD^d \left( \frac{\rho_{00}}{\rho_a} \right)^{0.4} \quad (3)$$

It takes into account the Foote and Du Toit (1969) correction of the air density with  $\rho_{00}$  the air density at the reference pressure level  $P_{00}$ . All fixed parameters are described in Table 1.

130 It can be noticed that the use of a Gamma distribution does not require much computational effort and allows the maximal flexibility. The  $p^{th}$  moment of the law ( $M(p)$ ) is written as:

$$M(p) = \int_0^{\infty} D^p n(D) dD = N \frac{\Gamma(\nu + p/\alpha)}{\Gamma(\nu)}, \quad (4)$$

Then, the mixing ratio ( $r$ ) and the number concentration ( $N$ ) of any hydrometeor are defined respectively by:

$$r = \int_0^{\infty} m(D) n(D) dD = aNM(b), \quad (5)$$

135 and:

$$N = \int_0^{\infty} n(D) dD = M(0). \quad (6)$$

The different processes involved in the evolution of the mixing ratio and number concentration of all hydrometeor categories are described in Table 2. The microphysical scheme is sketched in Figure 1 where each box represents a different category of water substance. In summary, cloud droplets are initiated following the activation scheme (HENU) as described in Cohard et al. (1998). Once initiated, cloud droplets grow by condensation of water vapour (CND) or evaporate (EVAP) instantaneously to avoid supersaturation over water drops. Then accretion (ACC), autoconversion (AUTO), self-collection (SC) and drops break-up (BU) processes are put in place to initiate precipitating hydrometeors and make them grow. Raindrops evaporate (EVAP) as they fall below the cloud base. The full 2 moment warm scheme is described in Cohard and Pinty (2000a, b).

Two heterogeneous processes can initiate ice crystals: the formation of ice embryos on insoluble IFN in a supersaturated environment over ice (HIND), and the freezing by immersion of supercooled droplets issuing from partially soluble CCN (IFR). The homogeneous nucleation (HON) takes place when the temperature drops below  $-35^\circ\text{C}$ ; it depletes very rapidly the cloud droplets and raindrops. The original IFN nucleation scheme comes from Phillips et al. (2008, 2013) and the adaption to the LIMA constraints (IFN PSD) is given in Vié et al. (2016). In addition, LIMA has two parameterizations of secondary production of ice crystals: the rime splintering mechanism (Beheng, 1987), also known as the Hallett-Mossop process (HM), and the collisional break-up of big ice crystals (Hoarau et al., 2018b) as well as the raindrop shattering when freezing (following Lawson et al., 2015), both are releasable processes for the moment.

150 Ice crystals can experience growth by water vapour deposition or sublimation (DEP/SUB) depending on the level of saturation with respect to ice. Pristine ice crystals autoconversion (CNV) forms snow/aggregates. Then, raindrop contact freezing



(CFRZ) or heavy riming (HRIM) on the snowflakes is the primary source of graupel. Then a number of interactions between  
155 the different hydrometeors are taken into account and listed in Table 2 and Figure 1. When the temperature is warmer than the  
triple point temperature ( $T_t$ ), small ice crystals are immediately converted into cloud water (IMLT), and snow/aggregates are  
converted into graupel (CMEL) at a rate proportional to their partial melting following (Walko et al., 1995). Graupels melt by  
shedding all the liquid water into raindrops (SHED).

When hail category is activated, these particles originate from the graupel category, where the particles likely experience a  
160 wet growth mode.

### 3 The new full two-moment version of LIMA

Generally, LIMA v2.0 is an advanced version of the LIMA scheme as the first fully 2 moment microphysics scheme in LIMA  
family. Version 2.0 inherits the six water species of the LIMA v1.0 alongside their interactions, while includes additional  
processes and the prognostic equations of all hydrometeor number concentration in the ice phase. All the processes concerned  
165 by the new features described in this section are shown in Figure 1 marked with red color.

In concrete terms, LIMA v2.0 is based on v1.0. Specifically, for processes related to snow, graupel and hail already handled  
in LIMA v1.0, a new prognostic equation is added to the existing routines for handling number concentration transfer rates.  
For processes newly handled in version 2.0, typically the self-collection of snow, a new routine is created including the param-  
eterization of this process and called up in the LIMA monitor routine. The choice of LIMA version (v1.0 or v2.0, partial or full  
170 2-moment) is made directly in the model namelist. The number of prognostic moments for each hydrometeor type individually  
is done thanks to namelists variables which can be set to 1 or 2 (to forecast the mixing ratio only, or both the mixing ratio and  
number concentration). This newly developed code is included in the official version of Meso-NH starting from version 5-6-0.

#### 3.1 Collection/Coalescence processes parameterization

##### 3.1.1 General formulation

175 Developing a numerical scheme to adequately simulate the growth of ice particles by collection is a true difficult task. As in  
many bulk parameterizations, the continuous growth and a simple geometric sweep-out concept for the collection kernel is  
assumed. The main difference in the treatment of this process in the various microphysical schemes is reflected in how the  
positive fall velocity differences are handled (see the next section). Straka and Mansell (2005) approximated these differences  
using mean fall velocities, as in Wisner et al. (1972). Seifert et al. (2006) improved the Wisner-like approximation with the  
180 notion of characteristic fall velocity difference. Milbrandt and Yau (2005) introduced mass-weighted fall velocities based on  
Murakami (1990). Following Walko et al. (1995) and as in LIMA, the numerical solutions of integrals involving the collection  
kernels are precomputed in the  $[\lambda_x^{min}, \lambda_x^{max}]$  range (logarithmic scale in LIMA v2.0) and stored in look-up tables. A new tables  
are also generated specifically for the number concentrations in this new version.

The collection processes can be categorized in three groups depending on the number of species involved.



185 (I) In the most general case, a new species  $Z$  can be formed during the collection processes ( $COL$ ) involving species  $X$  and  $Y$ . This is associated with simultaneous collection and conversion processes, and can be related to conditions on the mixing ratios  $r_x$  and  $r_y$ . So the mixing ratio ( $\Delta_{COL}r_y$ ) and number concentration ( $\Delta_{COL}N_y$ ) tendencies of species  $Y$  (a loss for  $Y$ ) due to the mass collection of  $X$  are:

$$\Delta_{COL}r_y = \rho_a^{-1} \int_0^{\infty} \left\{ \int_0^{\infty} K(D_x, D_y) m_y(D_y) n_y(D_y) dD_y \right\} n_x(D_x) dD_x, \quad (7)$$

190 and:

$$\Delta_{COL}N_y = \rho_a^{-1} \int_0^{\infty} \left\{ \int_0^{\infty} K(D_x, D_y) n_y(D_y) dD_y \right\} n_x(D_x) dD_x. \quad (8)$$

The collection kernel  $K$  is defined by:

$$K(D_x, D_y) = \frac{\pi}{4} (D_x + D_y)^2 |v_x(D_x) - v_y(D_y)| E_{xy}, \quad (9)$$

195 with  $E_{xy}$  the collection efficiency. The mixing ratio and number concentration tendencies for  $X$  (a loss for  $X$ ) are estimated in a similar way, and we can find a similar expression for  $\Delta_{COL}r_x$  and  $\Delta_{COL}N_x$ . The mixing ratio tendency of species  $Z$  (a gain for  $Z$ ) is the sum of the  $X$  and  $Y$  losses ( $\Delta_{COL}r_x + \Delta_{COL}r_y$ ). The number concentration tendency of species  $Z$  is  $\Delta_{COL}N_y$ .

(II) When  $Z$  is identical to one of the initial species  $X$  or  $Y$ , the collection becomes a two component process, and so only one mixing ratio collection rate needs to be calculated:  $\Delta_{COL}r_y = -\Delta_{COL}r_x$ . In this case, the number concentration of species  $X$  or  $Y$  varies following Eq.(8).

205 (III) Collection processes can also be considered as two- or three-component processes when threshold diameters are introduced. For example, when species  $X$  is collected by species  $Y$ , species  $Y$  is converted into species  $Z$  if and only if the diameter  $D_y$  of  $Y$  is greater than a required value  $D_y^{lim}$ . In this case, only a fraction of species  $Y$  (generally the fraction with a diameter greater than the threshold diameter) is converted to species  $Z$  and must be removed from category  $Y$ . The mass of the remaining fraction of species  $Y$  increases according to a collection process between the two species  $X$  and  $Y$  (for instance the riming of aggregates process). So, the growth of  $Y$  from  $X$  is now:

$$\Delta_{COL}r_{x \rightarrow y} = \rho_a^{-1} \int_0^{D_y^{lim}} \left\{ \int_0^{\infty} K(D_x, D_y) m_x(D_x) n_x(D_x) dD_x \right\} n_y(D_y) dD_y, \quad (10)$$

and the growth of  $Z$  from both  $X$  and  $Y$  is:

$$\begin{aligned} \Delta_{COL}r_{y \rightarrow z} &= \rho_a^{-1} \int_0^{\infty} \left\{ \int_{D_y^{lim}}^{\infty} K(D_x, D_y) m_y(D_y) n_y(D_y) dD_y \right\} n_x(D_x) dD_x, \\ &= \Delta_{COL}r_y - \Delta_{COL}r_{x \rightarrow y} \end{aligned} \quad (11)$$



210 while  $\Delta_{\text{COL}} r_y$ , the total loss of  $Y$  is given by Eq.(7).

The number concentration tendencies are a loss of species  $X$  given by Eq.(8), and a loss of species  $Y$  equivalent to a gain of species  $Z$  following:

$$\begin{aligned} \Delta_{\text{COL}} N_{y \rightarrow z} &= -\Delta_{\text{COL}} N_z \\ &= \Delta_{\text{COL}} N_y - \Delta_{\text{COL}} N_{y \rightarrow x} \\ &= \rho_a^{-1} \int_0^{\infty} \left\{ \int_{D_y^{\text{lim}}}^{\infty} K(D_x, D_y) n_y(D_y) dD_y \right\} n_x(D_x) dD_x, \end{aligned} \quad (12)$$

215 This much more physically-based approach, however, requires a technically more complicated partial integration on the dimensional spectrum of at least one species to calculate mixing ratio trends.

For warm processes (ACC, SC) the Long (1974) parameterization is used (see Cohard and Pinty, 2000a).

### 3.1.2 Cases with particles of different falling speeds magnitude

220 The collection equations can be simplified when the terminal falling velocity of species  $X$  can be neglected in view of that of  $Y$  (for instance  $X$  represent the pristine ice crystals and  $Y$  graupel). Thus, the falling speed of species  $X$  in Eq.(9) can be legitimately ignored, and Eq.(7) is developed as follows:

$$\begin{aligned} \Delta_{\text{COL}} r_y &= \rho_a^{-1} \left( \frac{\rho_{00}}{\rho_{\text{dref}}} \right)^{0.4} \frac{\pi}{4} a_y E_{xy} \int_0^{\infty} \left\{ \int_0^{\infty} D_y^2 c_y D_y^{d_y} D_y^{b_y} n_y(D_y) dD_y \right\} n_x(D_x) dD_x, \\ &= \rho_a^{-1} \left( \frac{\rho_{00}}{\rho_{\text{dref}}} \right)^{0.4} \frac{\pi}{4} E_{xy} c_y \times \int_0^{\infty} a_y D_y^{2+d_y+b_y} n_y(D_y) dD_y \times \int_0^{\infty} n_x(D_x) dD_x, \\ &= \rho_a^{-1} \left( \frac{\rho_{00}}{\rho_{\text{dref}}} \right)^{0.4} \frac{\pi}{4} E_{xy} c_y \times a_y N_y M(2+d_y+b_y) \times N_x, \end{aligned} \quad (13)$$

and Eq.(7) adapted for species  $X$  becomes:

$$\begin{aligned} \Delta_{\text{COL}} r_x &= \rho_a^{-1} \left( \frac{\rho_{00}}{\rho_{\text{dref}}} \right)^{0.4} \frac{\pi}{4} E_{xy} c_y \times \int_0^{\infty} D_y^{2+d_y} n_y(D_y) dD_y \times \int_0^{\infty} a_x D_x^{b_x} n_x(D_x) dD_x, \\ &= \left( \frac{\rho_{00}}{\rho_{\text{dref}}} \right)^{0.4} \frac{\pi}{4} E_{xy} c_y \times N_y M(2+d_y) \times r_x. \end{aligned} \quad (14)$$

225 Similarly, for concentrations, we get:

$$\begin{aligned} \Delta_{\text{COL}} N_x &= \Delta_{\text{COL}} N_y, \\ &= \rho_a^{-1} \left( \frac{\rho_{00}}{\rho_{\text{dref}}} \right)^{0.4} \frac{\pi}{4} E_{xy} c_y N_y M(2+d_y) N_x, \\ &= \frac{N_x}{r_x} \Delta_{\text{COL}} r_x \end{aligned} \quad (15)$$

In many calculations, the falling velocity of ice crystals or cloud droplets is relatively small and thus can be ignored. This is the case for:





1. **Raindrop contact freezing (CFR)** where the collection efficiency is fixed to  $E_{ir} = 1$ .
- 230 2. **Ice crystals aggregation (AGG)** where the collection efficiency is  $E_{is} = 0.25 e^{0.05(T-T_i)}$  based on Kajikawa and Heymsfield (1989). This is consistent with the decrease of the sticking efficiency of the interacting solid crystals when the temperature is cooler than the water triple point temperature  $T_t$ .
3. **Partial riming of the cloud droplets (RIM)** where the approach of Farley et al. (1989) is used with the assumption that a conversion of aggregates into graupels may occur for riming aggregates of size larger than  $D_s^{lim} = 7$  mm. Thus, the  
235 change rates of the cloud droplet, ice crystal and graupel mass and number concentration by riming (RIM) are estimated using Eq.(10-12) with an efficiency  $E_{cs} = 1$ .
4. **Graupel dry growth (DRYG)** is the sum of individual collection processes that is:

$$\Delta_{DRYG}r_g = \Delta_{DRYG}r_c + \Delta_{DRYG}r_r + \Delta_{DRYG}r_i + \Delta_{DRYG}r_s. \quad (16)$$

240 While the graupel number concentration is held constant during this process, the number concentration of cloud droplets, rain drops, ice crystals and snow/aggregates decreases. Since the terminal falling speed of cloud water and ice crystals can be neglected compared to that of graupel, the rates of change for cloud water ( $\Delta_{DRYG}r_c$ ) and ice crystals ( $\Delta_{DRYG}r_i$ ) follow Eq.(13-15), with the following efficiencies:

$$E_{cg} = 1 \quad \text{and} \quad E_{ig} = 0.01 e^{0.1(T-T_i)} \quad (17)$$

245 For raindrops and snow/aggregates whose falling speed cannot be neglected compared to the graupel falling speed, the rate of change is detailed in the following.

### 3.1.3 Cases with particles of significant falling speeds

When both  $X$  and  $Y$  have significant falling speeds, it becomes difficult to solve the integral form of equation (9) and the numerical technique suggested by Ferrier (1994) has therefore been adopted. Equation (9) can be rewritten as:

$$\Delta_{COL}r_y = \frac{1}{\rho_a} \frac{\pi}{4} \left( \frac{\rho_{00}}{\rho_{dref}} \right)^{0.4} N_x N_y \Lambda_r(\lambda_x, \lambda_y) \Delta v_{xy}(\lambda_x, \lambda_y), \quad (18)$$

250 where

$$\Delta v_{xy} = a_y \Lambda_r(\lambda_x, \lambda_y)^{-1} \int_0^\infty \left\{ \int_0^\infty E_{xy} (D_x + D_y)^2 |c_x D_x^{d_x} - c_y D_y^{d_y}| D_y^{b_y} g(D_y) dD_y \right\} n(D_x) dD_x \quad (19)$$

The normalization factor  $\Lambda_r(\lambda_x, \lambda_y)$  is obtained by removing  $E_{xy}$  and the absolute falling speed difference in Eq.(19), thus leading to the formal expression:

$$\begin{aligned} \Lambda_r(\lambda_x, \lambda_y) &= \int_0^\infty \left\{ \int_0^\infty (D_x + D_y)^2 D_y^{b_y} g(D_y) dD_y \right\} g_x(D_x) dD_x \\ &= M_x(2)M_y(b_y) + 2M_x(1)M_y(1+b_y) + M_y(2+b_y). \end{aligned} \quad (20)$$



255 An expression similar to  $\Delta_{\text{COL}}r_y$  can be used for the number concentration:

$$\Delta_{\text{COL}}N_y = \frac{1}{\rho_a} \frac{\pi}{4} \left( \frac{\rho_{00}}{\rho_{\text{dref}}} \right)^{0.4} N_x N_y \Lambda_N(\lambda_x, \lambda_y) \Delta v_{N,xy}(\lambda_x, \lambda_y), \quad (21)$$

where

$$\Delta v_{N,xy} = \Lambda_N(\lambda_x, \lambda_y)^{-1} \int_0^\infty \left\{ \int_0^\infty E_{xy}(D_x + D_y)^2 |c_x D_x^{d_x} - c_y D_y^{d_y}| g_y(D_y) dD_y \right\} g_x(D_x) dD_x \quad (22)$$

and with:

$$\begin{aligned} \Lambda_N(\lambda_x, \lambda_y) &= \int_0^\infty \left\{ \int_0^\infty (D_x + D_y)^2 g_y(D_y) dD_y \right\} g_x(D_x) dD_x \\ &= M_x(2) + 2M_x(1)M_y(1) + M_y(2). \end{aligned} \quad (23)$$

Since  $\Delta v_{xy}$  (resp.  $\Delta v_{N,xy}$ ) is a function only of the local values of  $\lambda_x$  and  $\lambda_y$ , a two-dimensional look-up table is created that contains the numerical solutions of Eq.(19) (resp. Eq. 22) for a series of logarithmically spaced  $(\lambda_x, \lambda_y)$  pairs in the physically expected ranges  $[\lambda_x^{\text{min}}, \lambda_x^{\text{max}}]$  and  $[\lambda_y^{\text{min}}, \lambda_y^{\text{max}}]$ , respectively. Then, a bilinear interpolation with respect to the tabulated values of  $\lambda_x$  and  $\lambda_y$  is used to accurately estimate  $\Delta v_{xy}$  (resp.  $\Delta v_{N,xy}$ ). The following processes are concerned:

265 1. **Rain accretion on aggregates (ACC):** As with cloud droplet riming, it is assumed that the collection of small raindrops by an aggregate does not alter its structure, while the collection of larger raindrops transforms an aggregate into a graupel. Based on Ferrier (1994), the diameter beyond which raindrop-collecting aggregates are considered graupels ( $D_r^{\text{lim}}$ ) is defined by calculating the density of the newly formed aggregate-raindrop mixture ( $\rho_{sr}$ ) from:

$$\frac{\pi}{6} \rho_w D_r^3 + \frac{\pi}{6} \underbrace{\left[ a_s \frac{6}{\pi} D_s^{b_s-3} \right]}_{\rho_s} D_s^3 = \frac{\pi}{6} \rho_{sr} D_s^3, \quad (24)$$

270 where  $\rho_w$  is the liquid water density. If  $\rho_{sr} > 0.5(\rho_g + \rho_s)$ , the new particle is categorized as a graupel of density  $\rho_g$ . Since graupels are considered as quasi spheroids ( $b_g \sim 3$  in Table 1),  $D_r^{\text{lim}}$  can be expressed as:

$$D_r^{\text{lim}} = \left[ \frac{3(a_g - a_s D_s^{b_s-3})}{\pi \rho_w} \right]^{1/3} D_s. \quad (25)$$

275 2. **Graupel dry growth (DRYG):** Rates involving drops ( $\Delta_{\text{DRYG}}r_r$  in Eq.(16)) and snow/aggregate particles ( $\Delta_{\text{DRYG}}r_s$  in Eq.(16)) are estimated with different efficiencies that are:  $E_{cg} = E_{rg}$  and  $E_{ig} = E_{sg}$  as in Ferrier (1994) with revisions in Ferrier et al. (1995).

3. **Graupel and hail wet growth (WETG/WETH):** In LIMA v2.0, the treatment of the competing dry/wet growth (DRYG/WETG) regimes follows Lin et al. (1983). Hence, these processes are computed by integrals of the form of Eq.(14). Similarly, as for the dry growth mode:  $\Delta_{\text{WETG}}N_i$ ,  $\Delta_{\text{WETG}}N_s$  and  $\Delta_{\text{WETG}}N_c$  are estimated using Eq.(15) and (23). The raindrop number concentration is given by:  $\Delta_{\text{WETG}}N_r = \Delta_{\text{WETG}}r_r \times \frac{N_r}{r_r}$ .



280 The formation rate of the hail particles is derived from the WET and DRY growth modes of the graupel particles. The partial conversion of graupels into hailstones is then approximated by:

$$\Delta_{\text{WET}} r_h = \left( \frac{\partial r_g}{\partial t} \right)^* \times \frac{\text{DRY}}{\text{DRY} + \text{WET}} \quad (26)$$

where  $(\partial r_g / \partial t)^*$  is the sum of the  $r_g$  tendencies before the conversion into hail.

285 Once formed, hail particles develop exclusively in the wet growth mode. When cloud droplets and hail decrease below a threshold, hail is converted into graupel following a linear percent conversion rate. The same rate is applied to the number concentration.

4. **Snow self collection (SC)** is parameterized using a snow-snow collection efficiency similar to Milbrandt and Yau (2005):

$$E_{ss} = 0.05e^{0.1(T-T_t)}$$

### 3.2 Source/Sink terms other than collection

290 Based on the assumption that the mean particle mass does not change in many processes, the tendency equations for  $N$  can be expressed as a function of the mixing ratio tendencies.

1. **Conversion of primary ice crystal to form aggregates (CNV)** In LIMA v2.0, ice crystals to snow/aggregates conversion follows Harrington et al. (1995) parameterization:

$$\Delta_{\text{CNV}} N_i = \frac{\Delta_{\text{CNV}} r_i}{a D_t^b}, \quad (27)$$

295 where  $D_t$  is the threshold diameter from which ice crystals are converted into snow aggregates. Here, this threshold diameter is fixed at  $D_t = 125 \mu\text{m}$ . The gain of snow/aggregates number concentration rate in LIMA v2.0 is then given by:  $\Delta N_s = -\Delta N_i$ .

2. **Ice particle melting (XMLT)**: For graupel melting (GMLT) process, by analogy to the graupel wet growth mode, the water formed at the surface of particles is shed away to form raindrops. It is assumed that all the raindrops formed have a fixed diameter thus the number concentration tendency is:

$$\begin{aligned} \Delta_{\text{GMLT}} N_g &= -\Delta_{\text{GMLT}} N_r \\ &= \Delta_{\text{GMLT}} r_g \times \frac{\rho_a}{m_{0r}}, \end{aligned} \quad (28)$$

where  $m_{0r}$  is the mass of a 0.72 mm raindrop diameter.

The melting process of snow particles/aggregates (CMEL) is different from that of graupels. Tunnel experiments have shown that, at the onset of melting, water from melting aggregates is trapped in the interstices of their porous structure.

305 Melting aggregates therefore tend to become denser and bear a certain resemblance to mixed-phase graupels.



The melting process of snow particles/aggregates (CMEL) is different from that of graupels. Wind tunnel experiments have shown that, at the onset of melting, water from melting aggregates is trapped in the interstices of their porous structure. Melting aggregates therefore tend to become denser and bear a certain resemblance to mixed-phase graupels. Consequently, it is assumed that a the portion of melting aggregates composed of a mixture of water and aggregates which is dense enough to become a graupel is transferred into (melting) graupels at a rate  $\Delta_{\text{CMEL}}N_s$  proportional to  $\Delta_{\text{MLT}}N_s$ :

$$\Delta_{\text{CMEL}}N_s = \alpha_{S \rightarrow G} \Delta_{\text{MLT}}N_s. \quad (29)$$

and

$$\Delta_{\text{MLT}}N_s = \Delta_{\text{MLT}}r_s \times \frac{N_s}{r_s}, \quad (30)$$

In this scheme,  $\alpha_{S \rightarrow G}$  has a value of 2, meaning that an equal portion of solid ice and liquid water is required for a graupel-like structure to be built during aggregate melting.

3. **Sedimentation (SED):** The rates are computed separately for the mixing ratios and the number concentrations as in Cohard and Pinty (2000a), and now extended to the ice-phase hydrometeors. The "two-moment" sedimentation rates enable the size sorting during the fall of the particles.

## 4 3D case study of an idealized severe storm

### 4.1 Initial model set-up

A case of supercellular storm (Barthe et al., 2005) has been chosen to illustrate the impact of the mixed-phase full two-moment LIMA-v2.0 scheme on the development and structure of a deep convection cloud. The simulation of the 3D supercellular storm starts from the initial sounding of Klemp and Wilhelmson (1978). Convection is initiated by a warm bubble of 1.5 K and 10 km radius which is located in the planetary boundary layer, in the center of the domain. The simulation lasts 90 minutes. It is performed on a domain of  $200 \times 200 \times 60$  gridpoints with a grid spacing of 500 m on the horizontal and 250 m on the vertical. Horizontal and vertical velocities are advected with a fourth-order scheme centered on space and time associated with a leap-frog temporal scheme. The Piecewise Parabolic Method (Colella and Woodward, 1984) associated with a forward-in-time temporal scheme is used to advect meteorological and scalar variables. The time step is 3 s. A 3D turbulence scheme (Cuxart et al., 2000) is activated.

The Meso-NH model is used to examine the differences between a simulation using the improved and full 2-moment microphysics scheme (hereinafter referred to as LIMA2), and another one using the original partially 2-moment microphysics scheme (hereinafter referred to as LIMA). The LIMA and LIMA2 simulations are fed with a superposition of several aerosol modes, and aerosols number concentrations are state variables in the model. Each aerosol mode is defined by distinct nucleation properties, and can be used as CCN to form cloud droplets (following Cohard et al., 1998) or as IFN to form ice crystals



(following Phillips et al., 2013). In this study, a single CCN mode and a single IFN mode are used. The CCN concentration is constant between the ground and 1000m altitude and set to  $300 \times 10^6 \text{m}^{-3}$ . Then it decreases exponentially up to 10,000m where it reaches a constant value of  $10 \times 10^3 \text{m}^{-3}$ . The IFN concentration is homogeneous on the vertical and set to  $1000 \text{L}^{-1}$ .

## 4.2 Modeled storm evolution

340 First of all, the location of the maximum of precipitation is the same in both simulation ( $X= 46.5\text{km}$ ,  $Y= 49\text{km}$  in Figure 2). The area covered by the accumulated precipitation at the ground are quite similar ( $315 \text{ km}^2$  in LIMA and  $395 \text{ km}^2$  in LIMA2) in the two simulations. However, the maximum value of the accumulated precipitation is larger in LIMA2 (122 mm) than in LIMA (75 mm). Concerning hail, LIMA simulates a much larger area of accumulated hail precipitation than LIMA2 (98 vs  $53 \text{ km}^2$ ). The LIMA simulation shows that hail is spread over almost the same area as rain. Conversely, the LIMA2 simulation  
345 produces more localized hail precipitation, close to the maximum accumulated precipitation. The LIMA2 simulation produces a dramatically reduced accumulated hail precipitation at the ground compared to the LIMA simulation (3 mm in LIMA2 vs. 15 mm in LIMA). Although it is not possible to draw conclusions about the simulated amount of hail on the ground, the rather restricted location with the LIMA2 simulation is more in line with the conceptual schemes of Doswell III and Burgess (1993) (Figures 1 and 2).

350 The time evolution of the mean updraft and downdraft (mean vertical wind speed from 0 to 8km) shown in Figure 3 is used to compare the dynamics of the two modeled systems. The mean downdraft and updraft in the 2 simulations are very close up to 32 min. After 32 minutes, however, the differences between the two simulations are more pronounced: up to  $1 \text{ m s}^{-1}$  for the mean updraft between 32 and 50 minutes and  $1.5 \text{ m s}^{-1}$  for the 75% confidence. The downdraft reaches its mean maximum at the time when the hail precipitation reaches its maximum (40 min for LIMA as compared to 50 min for LIMA2). Although  
355 the mean maxima are similar for the two simulations, the maxima are lower for LIMA2. For the mean precipitation rates, the differences are significant. LIMA2 produces a clear peak around  $34 \text{ mm/h}$  between 26 and 28 minutes, while LIMA produces a peak around  $25 \text{ mm/h}$  between 22 and 34 minutes. The average precipitation rate then decreases in the two simulations and the two curves almost merge from 40 minutes onwards. From 50 minutes, the mean rainfall in the two simulations is low, in the order of a few mm/h. The most significant differences are in the average hail precipitation rates. In LIMA, hail particles start to  
360 reach the ground at 26 min and the hail rate increases very rapidly, reaching  $8 \text{ mm/h}$  after 44 minutes. Significant oscillations in the hail precipitation rate are observed in this simulation, with maxima at 30 ( $3.5 \text{ mm/h}$ ), 34 ( $4.5 \text{ mm/h}$ ), 44 ( $7.5 \text{ mm/h}$ ) and 56 min ( $6 \text{ mm/h}$ ). On the other hand, in the LIMA2 simulation, the hail precipitation rate starts at the same time, but increases much more slightly, reaching a peak of  $2 \text{ mm/h}$  at 48 min. After 70 min, there is virtually no hail reaching the ground in LIMA2. Thus, the precipitation rates indicate a significant difference in the microphysical state of the storm when using LIMA  
365 with a single moment parameterization of the snow aggregates, graupel or hail versus the use of a 2-moment parameterization of these species, while the dynamics of the storm does not differ significantly between the two simulations.

Now we look into modeled outcomes from the two simulations at certain different times. At 26 minute when maximum rainfall is about to come while hail yet reaches the ground, major dynamical features of the two modeled systems are quite



370 similar. The second one is at 42 minutes, before the maximum of hail precipitation, and when the mean updraft reaches a  
threshold value and the subsidence becomes more intense. Figure 4 shows the general state of the two simulations at the  
selected times (vertical lines Figure 3). After 26 minutes of simulation (Figure 4a and c), surface dynamics (red and blue solid  
lines) and height dynamics (red and blue dashed lines) are similar, although there are slight differences in the location and  
extent of subsidence. The differences become more pronounced after 42 minutes of simulation. Rainfall is more intense in  
375 LIMA2 (by a factor of about 2) with a significant reduction in hail (by a factor of about 10). Again, while uplift zones are  
similar over the first 4km and between 4 and 8km, subsidence zones are different. In the LIMA2 simulations, the subsidence  
zones are located upstream (with respect to the surface currents) over the first 4 km, whereas in LIMA2 they are centred on the  
hail precipitation. The cloud composition is detailed in the following figure (Figure 5) along the oblique axis.

Figure 5 summarizes the vertical distribution of all hydrometeors through the maximum updraft. Each pie chart shows how  
380 the total water content (liquid plus solid in color contours) is distributed among all hydrometeors. As shown in Figure 3, the  
maximum simulated vertical velocity is similar in both simulations after 26 minutes (Figure 5a and c). In the two simulations,  
the extension (vertical and horizontal) of the system is similar. However, there are marked differences observed in the cloud  
and rain liquid water mixing ratio occurring at sub-zero temperatures. The total liquid water mixing ratio reaches  $0.1 \text{ g kg}^{-1}$   
up to  $-30^\circ\text{C}$  in the LIMA2 simulation. In the LIMA simulation it barely reaches  $-20^\circ\text{C}$ . The proportion of raindrops mass  
385 up to  $-20^\circ\text{C}$  is much higher in the LIMA2 simulation, with proportions exceeding 75% at some grid points. In contrast, it  
rarely exceeds 25% around the  $0^\circ\text{C}$  isotherm in the LIMA simulation. These high rain drop simulated proportions in LIMA2  
are associated with advection of icy hydrometeors, reducing the amount of solid water under  $0.1 \text{ g kg}^{-1}$  even under negative  
temperatures. This reduces their collection by icy hydrometeors and allows liquid hydrometeors to grow by condensation or  
autoconversion. More than 50% of the total water mass at the top of the system consists of ice crystals in LIMA2, whereas  
390 snow is the majority in LIMA. Hail precipitation almost reaches the surface in higher proportions in LIMA than in LIMA2.

After 42 minutes of simulations (Figure 5 b and d), the vertical extent of the system is slightly larger in LIMA2 (about 1  
km). As also shown in Figure 5 a and c, LIMA2 has produced higher liquid water content at higher levels, and the top of the  
cloud is mainly composed of ice crystals in LIMA2 compared to snow in LIMA. Snow appears to be much more localised  
395 outside the lift zones in LIMA2, whereas it is present at almost all grid points above the  $0^\circ\text{C}$  isotherm in LIMA. Although hail  
precipitation at the ground extends over 5 km in both simulations, the proportion and mass of hail are lower in LIMA2. Thus,  
a larger fraction of the simulated hail remains in the cloud.

In the sections that follow, the average cloud composition is followed, attempting to explain the differences in the simulations  
by the different conversion rates of the hydrometeor species. The temporal evolution of the horizontal-mean mixing ratio of  
400 each vertical profile of hydrometeors for which the thickness of the precipitating hydrometeor is greater than 0.5 mm is shown  
in Figure 6. This threshold has been chosen in order to cover all the cloudy areas of the domain. The corresponding temporal  
evolution of the number concentrations vertical profiles are shown in Figure 7. The  $C\lambda^x$  relationship is used to diagnose the  
snow, graupel and hail number concentration ratios shown for the LIMA simulation.



Since the modifications of the scheme concern the ice phase, we comment on the differences between the two simulations  
405 in the ice phase. The differences in the liquid phase are only consequences of what is observed in the ice phase.

The first panel in Figure 6 (a and g) shows the mass mixing ratio of the ice crystals. During the early stage of the system,  
ice crystal growth is similar in both simulations. Ice crystals mixing ratio reaches  $0.01 \text{ g kg}^{-1}$  after 18 minutes at a height of  
about 5 km in the LIMA simulation. In the LIMA2 simulation, the mixing ratio reaches up to  $0.35 \text{ g kg}^{-1}$  after 20 minutes  
and reaches a second significant peak of  $0.3 \text{ g kg}^{-1}$  between 32 and 38 minutes around 9 km height. Although the number  
410 concentrations are similar for the first 30 minutes in LIMA and LIMA2, then the number mixing ratios are significantly higher  
in the LIMA2 simulation. Ice mass accumulates between 4 and 6 km up to 20 minutes in LIMA2, while in LIMA it seems  
to be consumed more easily. After about 30 minutes of the simulation, ice accumulates between 8 and 10 km, both in terms  
of mixing ratio and number concentration. But once again, this accumulation is much larger when all the hydrometeors are  
represented using the 2-moment LIMA2 parameterization.

415

Figure 5 shows that in LIMA2 the snow was located below ice crystal accumulation, mainly in the stratiform part at the end  
of the simulation. These successive layers inside convective systems are also observed by Barnes and Houze Jr. (2014). The  
vertical profiles of Figure 6 (b and h) confirm this observation. The onset is 6 min later and at an altitude of 6 km compared  
to 4 km in the LIMA simulation. The maximum of  $0.7 \text{ g kg}^{-1}$  is reached after 20 minutes in the LIMA simulation and then  
420 decreases rapidly (after 30 minutes) to about  $0.2 \text{ g kg}^{-1}$  by the end of the simulation. In LIMA2 it is about  $0.2 \text{ g kg}^{-1}$  after 26  
minutes of simulation and this value increases only up to  $0.4 \text{ g kg}^{-1}$  until 50 minutes. The snow aggregates are spread between  
3 and 10 km height in the LIMA simulation, but it is more concentrated between 4 and 8 km in LIMA2. In the corresponding  
mean number concentration profiles, the differences are much more pronounced due to the hypothesis made in the one-moment  
version of the code (more explanation below).

425 For graupel (Figure 6 c and i) and hail (Figure 6 d and j), the mean mixing ratio profiles are similar with respect to the  
initiation time and the vertical extent. However, the mixing ratios are much lower for graupel in 2-moments and higher for  
hail. For these two species, the associated number concentration profiles are lower compared to the diagnostic used in LIMA.  
Between 30 and 40 minutes and between 6 and 8 km, hail profiles are most distinct.

The main differences in cloud droplet vertical profiles are simulated between 20 and 40 minutes. Even if the maximal values  
430 are similar, the vertical extend of mixing ratio exceeding  $0.15 \text{ g kg}^{-1}$  is higher in LIMA2 than LIMA simulation. Whereas,  
after 20 minutes of simulation the main effect on the rain drops can be seen. At this point, more drops are simulated between  
4 and 6 km.

The mean vertical profiles of the conversion rates in Figure 8 provide a further explanation of the differences between the  
LIMA and LIMA2 simulations discussed above. The profiles represent the average transfers weighted by the mixing ratio when  
435 the system is initiated between 14 and 24 minutes of simulation. This figure shows the efficiency of the different non-collection  
processes as in Figure 1a (Figure 8a-d) and the average transfers for the processes involving collection (Figure 8e-h).

At system initiation, the non-collection processes involving ice crystals (Figure 8a) are similar for both simulations. We zoomed  
in on the process of converting ice crystals into snow (CNVS), which is the process that initiates the snow. The differences in



snow mixing ratios highlighted in the previous figures are therefore linked to the growth processes. Figure 8e shows that the aggregation of ice crystals on snow is less effective when the concentration is prognostic (LIMA2). The processes involving snow and graupel are much less effective in the LIMA2 simulation. This is true for all processes (collection and non-collection). There are several explanations for the differences between the LIMA and LIMA2 simulations. The first is the different dimensions of the snow, graupel and hail aggregates when the number concentration is prognostic. It can be seen from Figure 9 that for these three species, the concentrations associated with a given mixing ratio will vary around a more frequently encountered one, but that this concentration is distinct in particular for low snow and graupel mixing ratios and for high hail mixing ratios. Thus the dimensions of snow and graupel are often smaller for low contents in LIMA than LIMA2 simulation, leading to a reduction in the efficiency of the deposition or collection processes of the other species. Thus more water vapor remain available for deposition on ice crystals and hail where the process is more efficient in the LIMA2 simulation, leading to higher ice crystal mixing ratio seen on Figure 6. Another explanation for the different levels at which the maximum concentrations are simulated as shown in Figure 5, Figure 6 and Figure 7 can come from sedimentation, which takes into account the dimensions of the hydrometeors in LIMA2. For hail, for example, we can see in Figure 8d that sedimentation occurs in similar proportions for the two simulations, but that hail is carried down to the ground more quickly. This is not shown here but it has been verified that this is the case throughout the simulation. This explains why there seems to be more hail on average within the system but less precipitation in LIMA2. Subsequently, this hail, which will be represented under the 0° C isoline, will have more time to melt and will increase rainfall.

When comparing the airborne data of number concentrations to the mass mixing ratios of snow and graupel, the LIMA v2.0 scheme can reproduce well the variability of  $N - r$  occurrences in agreement with the observations. Indeed, at very low mixing ratios, very high number concentrations are assumed in the parameterization of the snow concentration in the 1-moment version of the scheme (Figure 9a). This is confirmed by the evolution of the maximum diagnosed number concentration (Figure 7) which is anti-correlated with the maximum snow mixing ratio. This actually resolves a known issue of single-moment scheme for the benefit of estimating the optical and radiative properties of the cloud. Nevertheless, the relationship found using airborne in-situ measurements in Taufour et al. (2018) for snow is representative of convective cases over southeastern France where and when the HyMeX campaign took place. It is expected that the orographic environment, the season and the weather patterns also influence the size distribution characteristics of the cloud particles. Consequently, these results should be interpreted with caution, and should not be generalized without further studies and simulations of real cases.

In conclusion, the consideration of prognostic number concentration in version 2.0 of LIMA initially slows down the formation of snow and graupel. Ice crystals, cloud water droplets and rain therefore accumulate between 4 and 6 km, whereas these hydrometeors were consumed by these two species in version 1. The use of a constant to determine the diagnostic concentration of snow and graupel in version 1 of the scheme is the main reason for this. The ice, droplets and rain accumulated between 4 and 6 km then interact with the snow, graupel and hail. The use of 2 moments for snow creates a real distinction between the ice crystals that accumulate on the upper part of the cloud (around 9 to 10 km) and the snow that is localised at lower levels.





The intensification of the rain when all the hydrometeors in the diagram are activated at the same time seems to come from the  
475 melting of the hail and graupel. Hail precipitation is therefore lower in this version.

The developments that have been carried out in order to be able to represent icy hydrometeors in version 2 of the micro-  
physics scheme are giving promising results for an idealized case. Indeed, the simulations of highly precipitating systems  
presented in Taufour et al. (2018) show precipitation accumulations that are lower than the observations. Therefore, the ac-  
480 centuation of these accumulations for our idealised case would allow for a better estimation of the amounts of water that are  
generated in these simulations.

## 5 Summary and Conclusions

A new full two-moment microphysics scheme, LIMA2, has been developed from the previous partial two-moment scheme  
LIMA implemented in the Meso-NH cloud-resolving model. The new scheme now integrates the equations of the number  
485 concentrations in addition to those of the corresponding mass mixing ratios. Six hydrometeor categories are considered with  
new features concerning especially the precipitating ice phase categories including snow-aggregates, graupel and hail. Conse-  
quently, additional conversion rates, specific to the number concentration equations, are introduced on the basis of the particle  
size distributions.

The LIMA v2.0 scheme is numerically stable and more physically based than LIMA. It is tested using the host model  
490 Meso-NH for an idealized deep convection case. The results show that LIMA v2.0 works satisfactorily and so brings an  
original support to the study of convective cloud structures up to the development of hailstorms. The inclusion of prognostic  
number concentrations of snow, graupel, and hail has significant influences on the microphysical structure and on the dynamical  
evolution of the clouds.

Generally speaking, adding number concentration as a second prognostic moment to calculate size-dependent microphysical  
495 conversions leads to an increase of the mass mixing ratio of small ice crystals inside clouds and a decrease of snow and graupel  
hydrometeors in comparison to the results produced by the former LIMA scheme. In-depth analyses of the microphysical  
processes affected by the newly added number concentrations of snow, graupel, and hailstone suggest different feedbacks  
between rain and ice phase hydrometeors when compared to the results obtained with a single-moment parameterization of  
snow, graupel and hail. Applying the full 2-moment microphysical scheme not only modifies the mass mixing ratio of these  
500 hydrometeors but also impacts on other hydrometeors mass mixing ratios and the altitudes at which the variety of hydrometeors  
is maximized. For instance, it introduces a better opportunity for both raindrops and hailstones to reach the ground earlier or  
to reinforce locally the precipitation. It is believed that increasing the decoupling between number concentrations and mixing  
ratios is the key to improve the skills of microphysics schemes. The snow aggregate particles seem to be the most affected  
hydrometeor. The single moment parameterization of snow in LIMA v1.0 is already known to lead to discrepancies with  
505 observations Taufour et al. (2018); Wurtz et al. (2021). Wurtz et al. (2023) develop a new diagnostic of the  $\lambda$ , leading to  
improvements in the diagnostic number concentration and associated processes.



510 Many numerical weather prediction models use diagnostics to estimate hail risks due to unsatisfactory results for hail parameterizations. However, in terms of accumulation and location of hail risks, our scheme shows a clear improvement according to Doswell III and Burgess (1993). In addition to the impact on precipitation totals, secondary parameters such as hydrometeor dimensions and reflectivities can be better estimated with a more detailed description of all hydrometeors. Due to technical constraints, these parameters are often available from measurements, but are difficult to parameterise in models. Comparisons with observations will be more accurate if these parameters are better estimated in the models. The two-moment parameterization impacts the simulated radar reflectivities in such a way that more variability in hydrometeor sizes allow more variability in the radar reflectivity. Even if it is hard and a little bit tedious to compare the computed reflectivities to mean observed vertical profiles, the results presented in this study evidence the need to check more precisely the contribution of the different types of hydrometeors. It is expected that exploiting multiple parameters (Doppler shift and polarization diversity) of radar measurements (Caumont et al., 2006; Brown et al., 2017), is the way to quantitatively assess the accuracy of microphysics schemes to treat the variability of the hydrometeor types. The polarimetric radar operator, similar to Augros et al. (2016), will soon be adapted to the new scheme. This will allow further evaluation of supercell characteristics.

520 The sensitivity of the scheme to the aerosol interactions (chemical composition and size distributions) with cloud microphysics, provides a solid basis for the study of the influence of atmospheric aerosols on the size of hailstones that reach the ground, which can be a major cause of damage to agriculture and property. Further studies following this direction with more carefully designated locations and timing for IFN entering the cloud can address the issues associated with the increase of aerosols due to a polluted environment or more specifically a targeted cloud seeding experiment. Nevertheless, more evaluations should be conducted, ideally with realistic cases that we are currently working on.

*Code availability.* The LIMA v2.0 scheme has been implemented in the 5.6 version of the Meso-NH code. This reference version is under the CeCILL-C license agreement and freely available at <http://mesonh.aero.obs-mip.fr/mesonh56> (last access: 20 March 2024). The complete code of Meso-NH v5-6-0 including LIMA v2.0 is available at <https://zenodo.org/doi/10.5281/zenodo.11393717>. This repository also contains namelists to run the idealized storm and python scripts to reproduce the figures of this manuscript.

530 *Author contributions.* M. T. coded the LIMA (v2.0) scheme with B. V., performed the simulations, prepared the figures and initiated the manuscript. J.-P. P. advised the development of the LIMA (v2.0) scheme through discussions with M. T. and C. B., and finalized a first version of the manuscript. C. W. raised the idea to develop the advanced LIMA (v2.0) scheme from the existing LIMA code in MesoNH. C. B., B. V. and C. W. corrected in deep the manuscript.

*Competing interests.* The contact author has declared that none of the authors has any competing interests.



535 *Acknowledgements.* This study was supported by Agence Nationale de la Recherche (ANR) of France under the “Programme d’Investissements d’Avenir” (ANR-18-MPGA-003 EUROACE), France. This work was also supported by ANR ICCARE under grant ANR-21-CE01-0006. Computations were partially performed on the 36-node cluster of Lab. d’Aérodologie. J.-P. Pinty wishes to acknowledge CALMIP (CALcul en MIDI-Pyrénées) of the University of Toulouse for access to the "Olympe" supercomputer where useful additional simulations could be performed.



## 540 References

- Augros, C., Caumont, O., Ducrocq, V., Gaussiat, N., and Tabary, P.: Comparisons between S-, C- and X-band polarimetric radar observations and convective-scale simulations of the HyMeX first special observing period, *Q. J. Roy. Meteor. Soc.*, 142, 347–362, <https://doi.org/10.1002/qj.2572>, 2016.
- Barnes, H. C. and Houze Jr., R. A.: Precipitation hydrometeor type relative to the mesoscale airflow in mature oceanic deep convection of the Madden-Julian Oscillation, *J. Geophys. Res.-Atmos.*, 119, 13,990–14,014, <https://doi.org/10.1002/2014JD022241>, 2014.
- 545 Barthe, C., Molinié, G., and Pinty, J.-P.: Description and first results of an explicit electrical scheme in a 3D cloud resolving model, *Atmos. Res.*, 76, 95 – 113, <https://doi.org/10.1016/j.atmosres.2004.11.021>, 2005.
- Bechtold, P., Bazile, E., Guichard, F., Mascart, P., and Richard, E.: A mass-flux convection scheme for regional and global models, *Q. J. R. Meteorol. Soc.*, 127, 869–886, <https://doi.org/10.1002/qj.49712757309>, 2001.
- 550 Beheng, K. D.: Microphysical properties of glaciating cumulus clouds: comparison of measurements with a numerical simulation, *J. Geophys. Res.-Atmos.*, 113, 1377–1381, <https://doi.org/10.1002/qj.49711347815>, 1987.
- Brown, B. R., Bell, M. M., and Thompson, G.: Improvements to the snow melting process in a partially double moment microphysics parameterization, *J. Adv. Model. Earth Sy.*, 9, 1150–1166, <https://doi.org/10.1002/2016MS000892>, 2017.
- Caumont, O., Ducrocq, V., Delrieu, G., Gosset, M., Pinty, J.-P., Parent du Château, J., Andrieu, H., Lemaître, Y., and Scialom, G.: A radar simulator for high-resolution nonhydrostatic models, *J. Atmos. Ocean. Technol.*, 23, 1049–1067, <https://doi.org/10.1175/JTECH1905.1>, 2006.
- 555 Christensen, M. W. and Stephens, G. L.: Microphysical and macrophysical responses of marine stratocumulus polluted by underlying ships: Evidence of cloud deepening, *J. Geophys. Res.-Atmos.*, 116, <https://doi.org/10.1029/2010JD014638>, 2011.
- Cohard, J.-M. and Pinty, J.-P.: A comprehensive two-moment warm microphysical bulk scheme. I: Description and tests, *Q. J. Roy. Meteor. Soc.*, 126, 1815–1842, <https://doi.org/10.1002/qj.49712656613>, 2000a.
- 560 Cohard, J.-M. and Pinty, J.-P.: A comprehensive two-moment warm microphysical bulk scheme. II: 2D experiments with a non-hydrostatic model, *Q. J. Roy. Meteor. Soc.*, 126, 1843–1859, <https://doi.org/10.1002/qj.49712656614>, 2000b.
- Cohard, J.-M., Pinty, J.-P., and Bedos, C.: Extending Twomey’s Analytical Estimate of Nucleated Cloud Droplet Concentrations from CCN Spectra, *J. Atmos. Sci.*, 55, 3348–3357, [https://doi.org/10.1175/1520-0469\(1998\)055<3348:ETSABO>2.0.CO;2](https://doi.org/10.1175/1520-0469(1998)055<3348:ETSABO>2.0.CO;2), 1998.
- 565 Colella, P. and Woodward, P. R.: The Piecewise Parabolic Method (PPM) for gas-dynamical simulations, *Journal of Computational Physics*, 54, 174–201, [https://doi.org/10.1016/0021-9991\(84\)90143-8](https://doi.org/10.1016/0021-9991(84)90143-8), 1984.
- Cotton, W. R., Tripoli, G. J., Rauber, R. M., and Mulvihill, E. A.: Numerical Simulation of the Effects of Varying Ice Crystal Nucleation Rates and Aggregation Processes on Orographic Snowfall, *J. Clim. Appl. Meteorol.*, 25, 1658–1680, [https://doi.org/10.1175/1520-0450\(1986\)025<1658:NSOTEO>2.0.CO;2](https://doi.org/10.1175/1520-0450(1986)025<1658:NSOTEO>2.0.CO;2), 1986.
- 570 Cuxart, J., Bougeault, P., and Redelsperger, J.-L.: A turbulence scheme allowing for mesoscale and large-eddy simulations, *Q. J. R. Meteorol. Soc.*, 126, 1–30, <https://doi.org/10.1002/qj.49712656202>, 2000.
- Dawson, D. T., Xue, M., Milbrandt, J. A., and Yau, M. K.: Comparison of Evaporation and Cold Pool Development between Single-Moment and Multimoment Bulk Microphysics Schemes in Idealized Simulations of Tornadic Thunderstorms, *Mon. Weather Rev.*, 138, 1152 – 1171, <https://doi.org/10.1175/2009MWR2956.1>, 2010.
- 575 Delanoë, J., Protat, A., Testud, J., Bouniol, D., Heymsfield, A. J., Bansemer, A., Brown, P. R. A., and Forbes, R. M.: Statistical properties of the normalized ice particle size distribution, *J. Geophys. Res.-Atmos.*, 110, <https://doi.org/10.1029/2004JD005405>, d10201, 2005.



- Delanoë, J., Heymsfield, A. J., Protat, A., Bansemmer, A., and Hogan, R. J.: Normalized particle size distribution for remote sensing application, *J. Geophys. Res.-Atmos.*, 119, 4204–4227, <https://doi.org/10.1002/2013JD020700>, 2014.
- 580 Doswell III, C. A. and Burgess, D. W.: Tornadoes and Tornadoic Storms: a Review of Conceptual Models, p. 161–172, American Geophysical Union (AGU), <https://doi.org/10.1029/GM079p0161>, 1993.
- Farley, R. D., Price, P. E., Orville, H. D., and Hirsch, J. H.: On the Numerical Simulation of Graupel/Hall Initiation via the Riming of Snow in Bulk Water Microphysical Cloud Models, *Journal of Applied Meteorology*, 28, 1128–1131, [https://doi.org/10.1175/1520-0450\(1989\)028<1128:OTNSOG>2.0.CO;2](https://doi.org/10.1175/1520-0450(1989)028<1128:OTNSOG>2.0.CO;2), 1989.
- 585 Ferrier, B. S., Tao, W.-K., and Simpson, J.: A Double-Moment Multiple-Phase Four-Class Bulk Ice Scheme. Part II: Simulations of Convective Storms in Different Large-Scale Environments and Comparisons with other Bulk Parameterizations, *J. Atmos. Sci.*, 52, 1001–1033, [https://doi.org/10.1175/1520-0469\(1995\)052<1001:ADMMPF>2.0.CO;2](https://doi.org/10.1175/1520-0469(1995)052<1001:ADMMPF>2.0.CO;2), 1995.
- Ferrier, S.: A Double-Moment Multiple-Phase Four-Class Bulk Ice Scheme. Part I: Description, *J. Atmos. Sci.*, 51, 249–280, [https://doi.org/10.1175/1520-0469\(1994\)051<0249:ADMMPF>2.0.CO;2](https://doi.org/10.1175/1520-0469(1994)051<0249:ADMMPF>2.0.CO;2), 1994.
- 590 Foote, G. B. and Du Toit, P. S.: Terminal Velocity of Raindrops Aloft, *J. Appl. Meteorol.*, 8, 249–253, [https://doi.org/10.1175/1520-0450\(1969\)008<0249:TVORA>2.0.CO;2](https://doi.org/10.1175/1520-0450(1969)008<0249:TVORA>2.0.CO;2), 1969.
- Goren, T. and Rosenfeld, D.: Satellite observations of ship emission induced transitions from broken to closed cell marine stratocumulus over large areas, *J. Geophys. Res.-Atmos.*, 117, <https://doi.org/10.1029/2012JD017981>, 2012.
- Hall, W. D.: A Detailed Microphysical Model Within a Two-Dimensional Dynamic Framework: Model Description and Preliminary Results, *J. Atmos. Sci.*, 37, 2486 – 2507, [https://doi.org/10.1175/1520-0469\(1980\)037<2486:ADMMWA>2.0.CO;2](https://doi.org/10.1175/1520-0469(1980)037<2486:ADMMWA>2.0.CO;2), 1980.
- 595 Harrington, J. Y., Meyers, M. P., Walko, R. L., and Cotton, W. R.: Parameterization of Ice Crystal Conversion Processes Due to Vapor Deposition for Mesoscale Models Using Double-Moment Basis Functions. Part I: Basic Formulation and Parcel Model Results, *J. Atmos. Sci.*, 52, 4344 – 4366, [https://doi.org/10.1175/1520-0469\(1995\)052<4344:POICCP>2.0.CO;2](https://doi.org/10.1175/1520-0469(1995)052<4344:POICCP>2.0.CO;2), 1995.
- 600 Heymsfield, A. J., Bansemmer, A., Field, P. R., Durden, S. L., Stith, J. L., Dye, J. E., Hall, W., and Grainger, C. A.: Observations and Parameterizations of Particle Size Distributions in Deep Tropical Cirrus and Stratiform Precipitating Clouds: Results from In Situ Observations in TRMM Field Campaigns, *J. Atmos. Sci.*, 59, 3457–3491, [https://doi.org/10.1175/1520-0469\(2002\)059<3457:OAPOPS>2.0.CO;2](https://doi.org/10.1175/1520-0469(2002)059<3457:OAPOPS>2.0.CO;2), 2002.
- Heymsfield, A. J., Schmitt, C., Bansemmer, A., and Twohy, C. H.: Improved Representation of Ice Particle Masses Based on Observations in Natural Clouds, *J. Atmos. Sci.*, 67, 3303–3318, <https://doi.org/10.1175/2010JAS3507.1>, 2010.
- Heymsfield, A. J., Schmitt, C., and Bansemmer, A.: Ice Cloud Particle Size Distributions and Pressure-Dependent Terminal Velocities from In Situ Observations at Temperatures from 0° to -86° C, *J. Atmos. Sci.*, 70, 4123–4154, <https://doi.org/10.1175/JAS-D-12-0124.1>, 2013.
- 605 Hoarau, T., Barthe, C., Tulet, P., Claeys, M., Pinty, J.-P., Bousquet, O., Delanoë, J., and Vié, B.: Impact of the Generation and Activation of Sea Salt Aerosols on the Evolution of Tropical Cyclone Dumile, *J. Geophys. Res.-Atmos.*, 123, 8813–8831, <https://doi.org/10.1029/2017JD028125>, 2018a.
- Hoarau, T., Pinty, J.-P., and Barthe, C.: A representation of the collisional ice break-up process in the two-moment microphysics LIMA v1.0 scheme of Meso-NH, *Geosci. Model Dev.*, 11, 4269–4289, <https://doi.org/10.5194/gmd-11-4269-2018>, 2018b.
- 610 Hogan, R. J. and Bozzo, A.: A Flexible and Efficient Radiation Scheme for the ECMWF Model, *J. Adv. Model. Earth Sy.*, 10, 1990–2008, <https://doi.org/10.1029/2018MS001364>, 2018.
- Kajikawa, M. and Heymsfield, A. J.: Aggregation of Ice Crystals in Cirrus, *J. Atmos. Sci.*, 46, 3108–3121, [https://doi.org/10.1175/1520-0469\(1989\)046<3108:AOICIC>2.0.CO;2](https://doi.org/10.1175/1520-0469(1989)046<3108:AOICIC>2.0.CO;2), 1989.



- 615 Khain, A., Ovtchinnikov, M., Pinsky, M., Pokrovsky, A., and Krugliak, H.: Notes on the state-of-the-art numerical modeling of cloud micro-  
physics, *Atmos. Res.*, 55, 159–224, [https://doi.org/https://doi.org/10.1016/S0169-8095\(00\)00064-8](https://doi.org/https://doi.org/10.1016/S0169-8095(00)00064-8), 2000.
- Khairoutdinov, M. and Kogan, Y.: A New Cloud Physics Parameterization in a Large-Eddy Simulation Model of Marine Stratocumulus, *Mon. Weather Rev.*, 128, 229–243, [https://doi.org/10.1175/1520-0493\(2000\)128<0229:ANCPPI>2.0.CO;2](https://doi.org/10.1175/1520-0493(2000)128<0229:ANCPPI>2.0.CO;2), 2000.
- Klemp, J. B. and Wilhelmson, R. B.: The Simulation of Three-Dimensional Convective Storm Dynamics, *J. Atmos. Sci.*, 35, 1070–1096, [https://doi.org/10.1175/1520-0469\(1978\)035<1070:TSOTDC>2.0.CO;2](https://doi.org/10.1175/1520-0469(1978)035<1070:TSOTDC>2.0.CO;2), 1978.
- 620 Lac, C., Chaboureaud, J.-P., Masson, V., Pinty, J.-P., Tulet, P., Escobar, J., Leriche, M., Barthe, C., Aouizerats, B., Augros, C., Aumond, P.,  
Auguste, F., Bechtold, P., Berthet, S., Bieilli, S., Bosseur, F., Caumont, O., Cohard, J.-M., Colin, J., Couvreux, F., Cuxart, J., Delautier, G.,  
Dauhut, T., Ducrocq, V., Filippi, J.-B., Gazen, D., Geoffroy, O., Gheusi, F. and Honnert, R., Lafore, J.-P., Lebeaupin Brossier, C., Libois,  
Q., Lunet, T., Mari, C., Maric, T., Mascart, P., Mogé, M., Molinié, G., Nuissier, O., Pantillon, F., Peyrillé, P., Pergaud, J., Perraud, E.,  
Pianezze, J., Redelsperger, J.-L., Ricard, D., Richard, E., Riette, S., Rodier, Q., Schoetter, R., Seyfried, L., Stein, J., Suhre, K., Taufour,  
625 M., Thouron, O., Turner, S., Verrelle, A., Vié, B., Visentin, F., Vionnet, V., and Wautelet, P.: Overview of the Meso-NH model version 5.4  
and its applications, *Geosci. Model Dev.*, 11, 1929–1969, <https://doi.org/10.5194/gmd-11-1929-2018>, 2018.
- Lafore, J. P., Stein, J., Asencio, N., Bougeault, P., Ducrocq, V., Duron, J., Fischer, C., Hérelil, P., Mascart, P., Masson, V., Pinty, J. P.,  
Redelsperger, J. L., Richard, E., and Vilà-Guerau de Arellano, J.: The Meso-NH Atmospheric Simulation System. Part I: adiabatic formu-  
lation and control simulations, *Ann. Geophys.*, 16, 90–109, <https://doi.org/10.1007/s00585-997-0090-6>, 1998.
- 630 Lau, K., Kim, M., and Kim, K.: Asian summer monsoon anomalies induced by aerosol direct forcing: the role of the Tibetan Plateau, *Clim.*  
*Dynam.*, 26, 855–864, <https://doi.org/10.1007/s00382-006-0114-z>, 2006.
- Lawson, R. P., Woods, S., and Morrison, H.: The Microphysics of Ice and Precipitation Development in Tropical Cumulus Clouds, *J. Atmos.*  
*Sci.*, 72, 2429 – 2445, <https://doi.org/10.1175/JAS-D-14-0274.1>, 2015.
- Lee, S. S.: Effect of Aerosol on Circulations and Precipitation in Deep Convective Clouds, *J. Atmos. Sci.*, 69, 1957–1974,  
635 <https://doi.org/10.1175/JAS-D-11-0111.1>, 2012.
- Lin, Y.-L., Farley, R. D., and Orville, H. D.: Bulk Parameterization of the Snow Field in a Cloud Model, *J. Clim. Appl. Meteorol.*, 22,  
1065–1092, [https://doi.org/10.1175/1520-0450\(1983\)022<1065:BPOTSF>2.0.CO;2](https://doi.org/10.1175/1520-0450(1983)022<1065:BPOTSF>2.0.CO;2), 1983.
- Long, A. B.: Solutions to the Droplet Collection Equation for Polynomial Kernels, *J Atmos. Sci.*, 31, 1040 – 1052,  
[https://doi.org/10.1175/1520-0469\(1974\)031<1040:STTDCE>2.0.CO;2](https://doi.org/10.1175/1520-0469(1974)031<1040:STTDCE>2.0.CO;2), 1974.
- 640 Masson, V., Le Moigne, P., Martin, E., Faroux, S., Alias, A., Alkama, R., Belamari, S., Barbu, A., Boone, A., Bouysse, F., Brousseau, P.,  
Brun, E., Calvet, J.-C., Carrer, D., Decharme, B., Delire, C., Donier, S., Essaouini, K., Gibelin, A.-L., Giordani, H., Habets, F., Jidane, M.,  
Kerdran, G., Kourzeneva, E., Lafaysse, M., Lafont, S., Lebeaupin Brossier, C., Lemonsu, A., Mahfouf, J.-F., Marguinaud, P., Mokhtari,  
M., Morin, S., Pigeon, G., Salgado, R., Seity, Y., Taillefer, F., Tanguy, G., Tulet, P., Vincendon, B., Vionnet, V., and Voldoire, A.: The  
SURFEXv7.2 land and ocean surface platform for coupled or offline simulation of Earth surface variables and fluxes, *Geosci. Model Dev.*,  
645 6, 929–960, <https://doi.org/10.5194/gmd-6-929-2013>, 2013.
- McFarquhar, G. M., Baumgardner, D., Bansemer, A., Abel, S. J., Crosier, J., French, J., Rosenberg, P., Korolev, A., Schwarzenboeck, A.,  
Leroy, D., Um, J., Wu, W., Heymsfield, A. J., Twohy, C., Detwiler, A., Field, P., Neumann, A., Cotton, R., Axisa, D., and Dong, J.:  
Processing of Ice Cloud In Situ Data Collected by Bulk Water, Scattering, and Imaging Probes: Fundamentals, Uncertainties, and Efforts  
toward Consistency, *Meteor. Mon.*, 58, 11.1–11.33, <https://doi.org/10.1175/amsmonographs-d-16-0007.1>, 2017.
- 650 Meyers, M. P., Walko, R. L., Harrington, J. Y., and Cotton, W. R.: New RAMS cloud microphysics parameterization. Part II: The two-moment  
scheme, *Atmos. Res.*, 45, 3 – 39, [https://doi.org/10.1016/S0169-8095\(97\)00018-5](https://doi.org/10.1016/S0169-8095(97)00018-5), 1997.

Milbrandt, J. A. and Yau, M. K.: A Multimoment Bulk Microphysics Parameterization. Part II: A Proposed Three-Moment Closure and Scheme Description, *J. Atmos. Sci.*, 62, 3065–3081, <https://doi.org/10.1175/JAS3535.1>, 2005.

655 Milbrandt, J. A. and Yau, M. K.: A Multimoment Bulk Microphysics Parameterization. Part III: Control Simulation of a Hailstorm, *J. Atmos. Sci.*, 63, 3114 – 3136, <https://doi.org/10.1175/JAS3816.1>, 2006.

Milbrandt, J. A., Yau, M. K., Mailhot, J., Bélair, S., and McTaggart-Cowan, R.: Simulation of an Orographic Precipitation Event during IMPROVE-2. Part II: Sensitivity to the Number of Moments in the Bulk Microphysics Scheme, *Mon. Weather Rev.*, 138, 625 – 642, <https://doi.org/10.1175/2009MWR3121.1>, 2010.

660 Mlawer, E. J., Taubman, S. J., Brown, P. D., Iacono, M. J., and Clough, S. A.: Radiative transfer for inhomogeneous atmospheres: RRTM, a validated correlated-k model for the longwave, *J. Geophys. Res.-Atmos.*, 102, 16 663–16 682, <https://doi.org/10.1029/97JD00237>, 1997.

Morcrette, J.-J.: Radiation and cloud radiative properties in the European Centre for Medium Range Weather Forecasts forecasting system, *J. Geophys. Res.-Atmos.*, 96, 9121–9132, <https://doi.org/10.1029/89JD01597>, 1991.

665 Morrison, H., Thompson, G., and Tatarskii, V.: Impact of Cloud Microphysics on the Development of Trailing Stratiform Precipitation in a Simulated Squall Line: Comparison of One- and Two-Moment Schemes, *Mon. Weather Rev.*, 137, 991–1007, <https://doi.org/10.1175/2008MWR2556.1>, 2009.

Murakami, M.: Numerical Modeling of Dynamical and Microphysical Evolution of an Isolated Convective Cloud, *Journal of the Meteorological Society of Japan. Ser. II*, 68, 107–128, [https://doi.org/10.2151/jmsj1965.68.2\\_107](https://doi.org/10.2151/jmsj1965.68.2_107), 1990.

670 Nickerson, E. C., Richard, E., Rosset, R., and Smith, D. R.: The Numerical Simulation of Clouds, Rains and Airflow over the Vosges and Black Forest Mountains: A Meso- $\beta$  Model with Parameterized Microphysics, *Mon. Weather Rev.*, 114, 398–414, [https://doi.org/10.1175/1520-0493\(1986\)114<0398:TNSOCR>2.0.CO;2](https://doi.org/10.1175/1520-0493(1986)114<0398:TNSOCR>2.0.CO;2), 1986.

Noppel, H., Blahak, U., Seifert, A., and Beheng, K. D.: Simulations of a hailstorm and the impact of CCN using an advanced two-moment cloud microphysical scheme, *Atmos. Res.*, 96, 286 – 301, <https://doi.org/10.1016/j.atmosres.2009.09.008>, 2010.

Pergaud, J., Masson, V., Malardel, S., and Couvreux, F.: A Parameterization of Dry Thermals and Shallow Cumuli for Mesoscale Numerical Weather Prediction, *Bound.-Lay. Meteorol.*, 132, 83, <https://doi.org/10.1007/s10546-009-9388-0>, 2009.

675 Phillips, V. T. J., DeMott, P. J., and Andronache, C.: An Empirical Parameterization of Heterogeneous Ice Nucleation for Multiple Chemical Species of Aerosol, *J. Atmos. Sci.*, 65, 2757–2783, <https://doi.org/10.1175/2007JAS2546.1>, 2008.

Phillips, V. T. J., Demott, P. J., Andronache, C., Pratt, K. A., Prather, K. A., Subramanian, R., and Twohy, C.: Improvements to an Empirical Parameterization of Heterogeneous Ice Nucleation and Its Comparison with Observations, *J. Atmos. Sci.*, 70, 378–409, <https://doi.org/10.1175/JAS-D-12-080.1>, 2013.

680 Pianezze, J., Barthe, C., Bielli, S., Tulet, P., Jullien, S., Cambon, G., Bousquet, O., Claeys, M., and Cordier, E.: A New Coupled Ocean-Waves-Atmosphere Model Designed for Tropical Storm Studies: Example of Tropical Cyclone Bejisa (2013–2014) in the South-West Indian Ocean, *J. Adv. Model. Earth Sy.*, 10, 801–825, <https://doi.org/10.1002/2017MS001177>, 2018.

685 Pinty, J. P. and Jabouille, P.: A mixed-phase cloud parameterization for use in mesoscale non hydrostatic model: simulations of a squall line and of orographic precipitations, in: *Proceedings of Conf. on Cloud Physics*, pp. 217–220, Amer. Meteor. Soc Everett, WA, <https://worldcat.org/oclc/39920280>, 1998.

Pruppacher, H. and Klett, J.: *Microphysics of Clouds and Precipitation*, Kluwer Academic Publishers, Dordrecht, The Netherlands, <https://doi.org/10.1007/978-0-306-48100-0>, 1997.

Reisner, J., Rasmussen, R. M., and Bruintjes, R. T.: Explicit forecasting of supercooled liquid water in winter storms using the MM5 mesoscale model, *Q. J. R. Meteorol. Soc.*, 124, 1071–1107, <https://doi.org/10.1002/qj.49712454804>, 1998.



- 690 Schnaiter, M., Järvinen, E., Vochezer, P., Abdelmonem, A., Wagner, R., Jourdan, O., Mioche, G., Sheherbakov, V. N., Schmitt, C. G., Tricoli, U., Ulanowski, Z., and Heymsfield, A. J.: Cloud chamber experiments on the origin of ice crystal complexity in cirrus clouds, *Atmos Chem. Phys.*, 16, 5091–5110, <https://doi.org/10.5194/acp-16-5091-2016>, 2016.
- Seifert, A. and Beheng, K.: A two-moment cloud microphysics parameterization for mixed-phase clouds. Part 2: Maritime vs. continental deep convective storms, *Meteorol. Atmos. Phys.*, 92, 67–82, <https://doi.org/10.1007/s00703-005-0113-3>, 2006a.
- 695 Seifert, A. and Beheng, K. D.: A two-moment cloud microphysics parameterization for mixed-phase clouds. Part 1: Model description, *Meteorol. Atmos. Phys.*, 92, 45–66, <https://doi.org/10.1007/s00703-005-0112-4>, 2006b.
- Seifert, A., Khain, A., Pokrovsky, A., and Beheng, K. D.: A comparison of spectral bin and two-moment bulk mixed-phase cloud microphysics, *Atmos. Res.*, 80, 46–66, <https://doi.org/10.1016/j.atmosres.2005.06.009>, 2006.
- Simpson, E. L., Connolly, P. J., and McFiggans, G.: Competition for water vapour results in suppression of ice formation in mixed-phase clouds, *Atmospheric Chemistry and Physics*, 18, 7237–7250, <https://doi.org/10.5194/acp-18-7237-2018>, 2018.
- 700 Simpson, J.: *Cumulus Clouds: Interactions Between Laboratory Experiments and Observations as Foundations for Models*, pp. 399–412, Springer Netherlands, Dordrecht, ISBN 978-94-017-2241-4, [https://doi.org/10.1007/978-94-017-2241-4\\_22](https://doi.org/10.1007/978-94-017-2241-4_22), 1983.
- Srivastava, R. C.: Parameterization of Raindrop Size Distributions, *J. Atmos. Sci.*, 35, 108–117, [https://doi.org/10.1175/1520-0469\(1978\)035<0108:PORSDD>2.0.CO;2](https://doi.org/10.1175/1520-0469(1978)035<0108:PORSDD>2.0.CO;2), 1978.
- 705 Straka, J. M. and Mansell, E. R.: A Bulk Microphysics Parameterization with Multiple Ice Precipitation Categories, *J. Appl. Meteor.*, 44, 445–466, <https://doi.org/10.1175/JAM2211.1>, 2005.
- Tao, W.-K., Chen, J.-P., Li, Z., Wang, C., and Zhang, C.: Impact of aerosols on convective clouds and precipitation, *Rev. Geophys.*, 50, <https://doi.org/10.1029/2011RG000369>, 2012.
- Taufour, M., Vié, B., Augros, C., Boudevillain, B., Delanoë, J., Delautier, G., Ducrocq, V., Lac, C., Pinty, J.-P., and Schwarzenböck, A.: Evaluation of the two-moment scheme LIMA based on microphysical observations from the HyMeX campaign, *Q. J. R. Meteorol. Soc.*, 144, 1398–1414, <https://doi.org/10.1002/qj.3283>, 2018.
- 710 Thompson, G., Rasmussen, R. M., and Manning, K.: Explicit forecasts of winter precipitation using an improved bulk microphysics scheme. Part I: Description and sensitivity analysis, *Mon. Weather Rev.*, 132, 519–542, [https://doi.org/10.1175/1520-0493\(2004\)132<0519:EFOWPU>2.0.CO;2](https://doi.org/10.1175/1520-0493(2004)132<0519:EFOWPU>2.0.CO;2), 2004.
- 715 van den Heever, S. C., Stephens, G. L., and Wood, N. B.: Aerosol Indirect Effects on Tropical Convection Characteristics under Conditions of Radiative–Convective Equilibrium, *J. Atmos. Sci.*, 68, 699–718, <https://doi.org/10.1175/2010JAS3603.1>, 2011.
- Vié, B., Pinty, J.-P., Berthet, S., and Leriche, M.: LIMA (v1.0): A quasi two-moment microphysical scheme driven by a multimodal population of cloud condensation and ice freezing nuclei, *Geosci. Model Dev.*, 9, 567–586, <https://doi.org/10.5194/gmd-9-567-2016>, 2016.
- Voldoire, A., Decharme, B., Pianezze, J., Lebeaupin Brossier, C., Sevault, F., Seyfried, L., Garnier, V., Bielli, S., Valcke, S., Alias, A., Accensi, M., Arduin, F., Bouin, M.-N., Ducrocq, V., Faroux, S., Giordani, H., Léger, F., Marsaleix, P., Rainaud, R., Redelsperger, J.-L., Richard, E., and Riette, S.: SURFEX v8.0 interface with OASIS3-MCT to couple atmosphere with hydrology, ocean, waves and sea-ice models, from coastal to global scales, *Geosci. Model Dev.*, 10, 4207–4227, <https://doi.org/10.5194/gmd-10-4207-2017>, 2017.
- 720 Walko, R., Cotton, W., Meyers, M., and Harrington, J.: New RAMS cloud microphysics parameterization part I: the single-moment scheme, *Atmos. Res.*, 38, 29 – 62, [https://doi.org/10.1016/0169-8095\(94\)00087-T](https://doi.org/10.1016/0169-8095(94)00087-T), 1995.
- 725 Wang, C. and Chang, J. S.: A three-dimensional numerical model of cloud dynamics, microphysics, and chemistry: 1. Concepts and formulation, *J. Geophys. Res.-Atmos.*, 98, 14 827–14 844, <https://doi.org/10.1029/92JD01393>, 1993.





- Wang, P. K. and Ji, W.: Collision Efficiencies of Ice Crystals at Low–Intermediate Reynolds Numbers Colliding with Supercooled Cloud Droplets: A Numerical Study, *J. Atmos. Sci.*, 57, 1001 – 1009, [https://doi.org/10.1175/1520-0469\(2000\)057<1001:CEOICA>2.0.CO;2](https://doi.org/10.1175/1520-0469(2000)057<1001:CEOICA>2.0.CO;2), 2000.
- 730 Wisner, C., Orville, H. D., and Myers, C.: A Numerical Model of a Hail-Bearing Cloud, *J. Atmos. Sci.*, 29, 1160–1181, [https://doi.org/10.1175/1520-0469\(1972\)029<1160:ANMOAH>2.0.CO;2](https://doi.org/10.1175/1520-0469(1972)029<1160:ANMOAH>2.0.CO;2), 1972.
- Wurtz, J., Bouniol, D., Vié, B., and Lac, C.: Evaluation of the AROME model’s ability to represent ice crystal icing using in situ observations from the HAIC 2015 field campaign, *Q. J. R. Meteorol. Soc.*, 147, 2796–2817, <https://doi.org/10.1002/qj.4100>, 2021.
- Wurtz, J., Bouniol, D., and Vié, B.: Improvements to the parametrization of snow in AROME in the context of ice crystal icing, *Q. J. R. Meteorol. Soc.*, 149, 878–893, <https://doi.org/10.1002/qj.4437>, 2023.
- 735 Ziegler, C. L.: Retrieval of Thermal and Microphysical Variables in Observed Convective Storms. Part 1: Model Development and Preliminary Testing, *Journal of the Atmospheric Sciences*, 42, 1487–1509, [https://doi.org/10.1175/1520-0469\(1985\)042<1487:ROTAMV>2.0.CO;2](https://doi.org/10.1175/1520-0469(1985)042<1487:ROTAMV>2.0.CO;2), 1985.

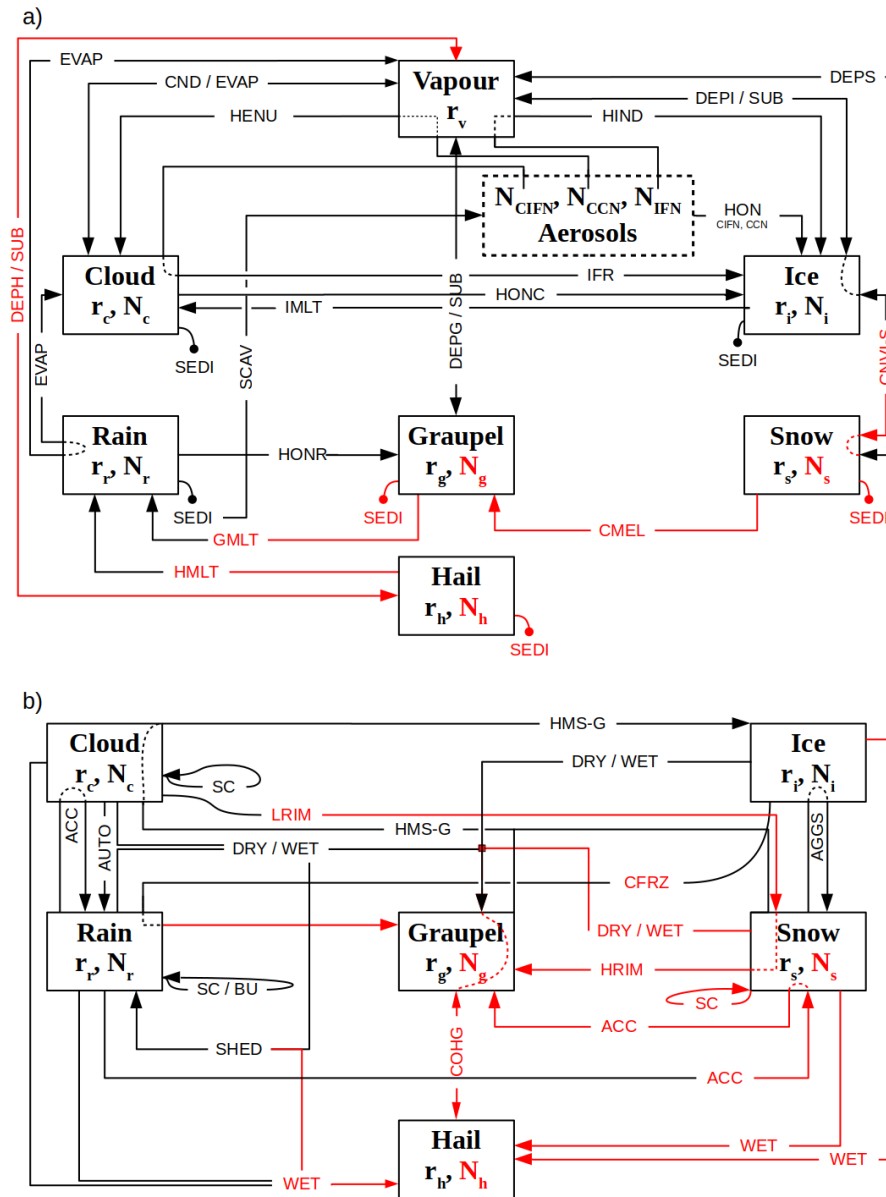


**Figure 1.** Diagrams of the microphysical processes of LIMA v2.0 representing all the processes except collection (a) and all the collection processes (b). Red arrows represent new or modified processes in v2.0, black arrows are identical processes in LIMA v1.0 and v2.0. Prognostic variables for all the hydrometeor species are written in the boxes, with  $r_x$  and  $N_x$  the mixing ratio and number concentration of the species  $x$ , respectively. The process label are explained in Table 2.

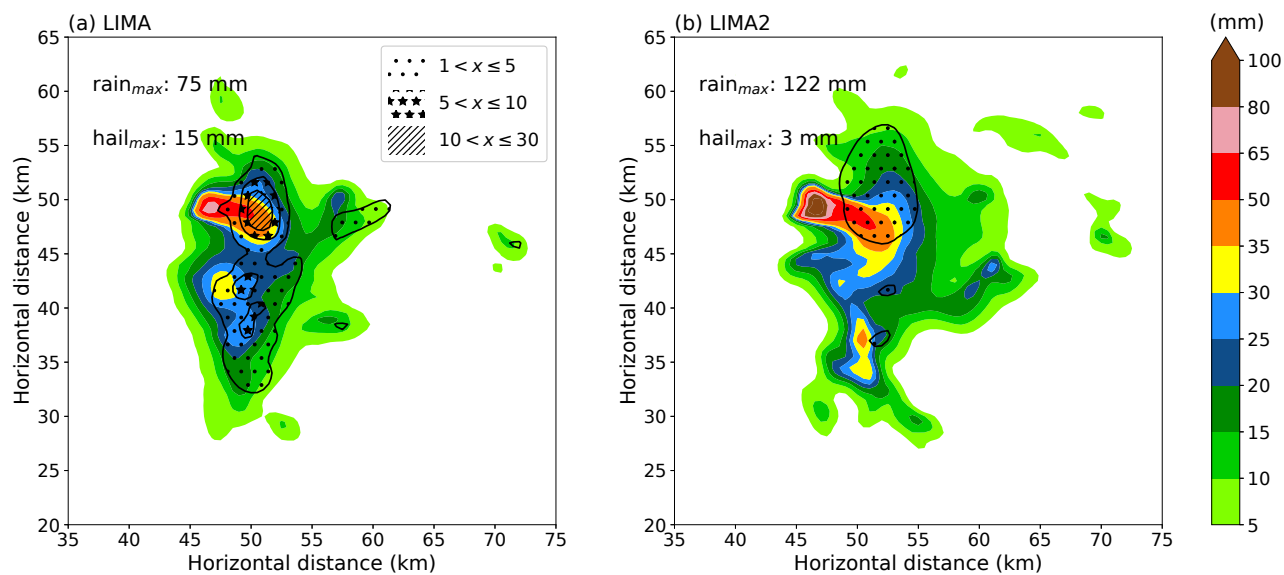


**Figure 2.** Accumulated precipitation (mm) from rain (colors) and hail (lines) at the ground for the (a) LIMA and (b) LIMA2 simulations.

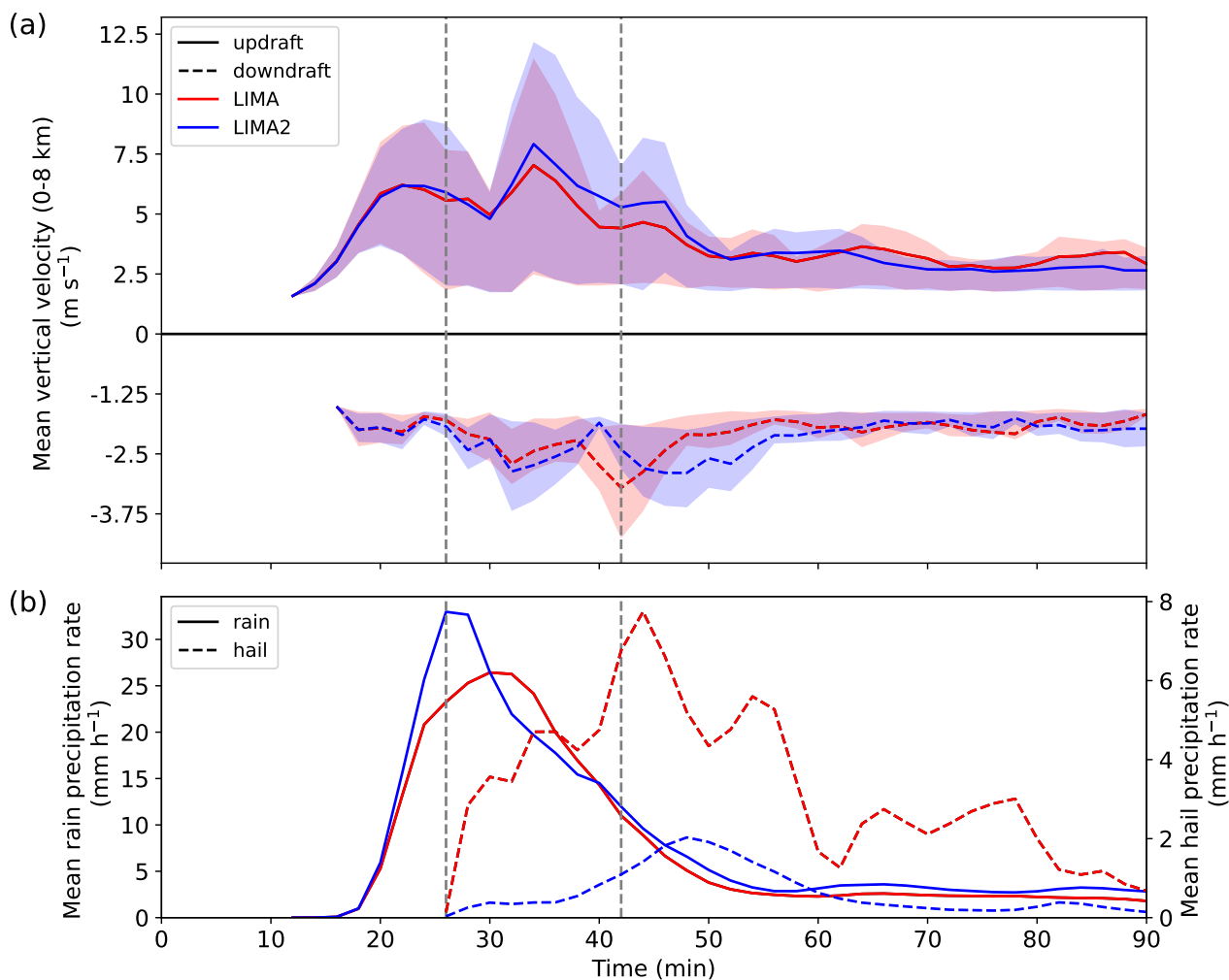


**Figure 3.** Temporal evolution of vertical motions (a) and precipitation rates at the ground (b). In (a), the domain mean vertical updraft speed between the surface and 8km altitude (top) is represented by the solid lines, and the mean downdraft (bottom) is plotted with dashed lines. The interquartile range is represented in shading. In (b), the mean rain rate of rainy area at the ground is plotted with solid lines and the mean hail rate is plotted with dashed lines. The vertical dashed lines correspond to the time when sections in Figure 5 are shown.

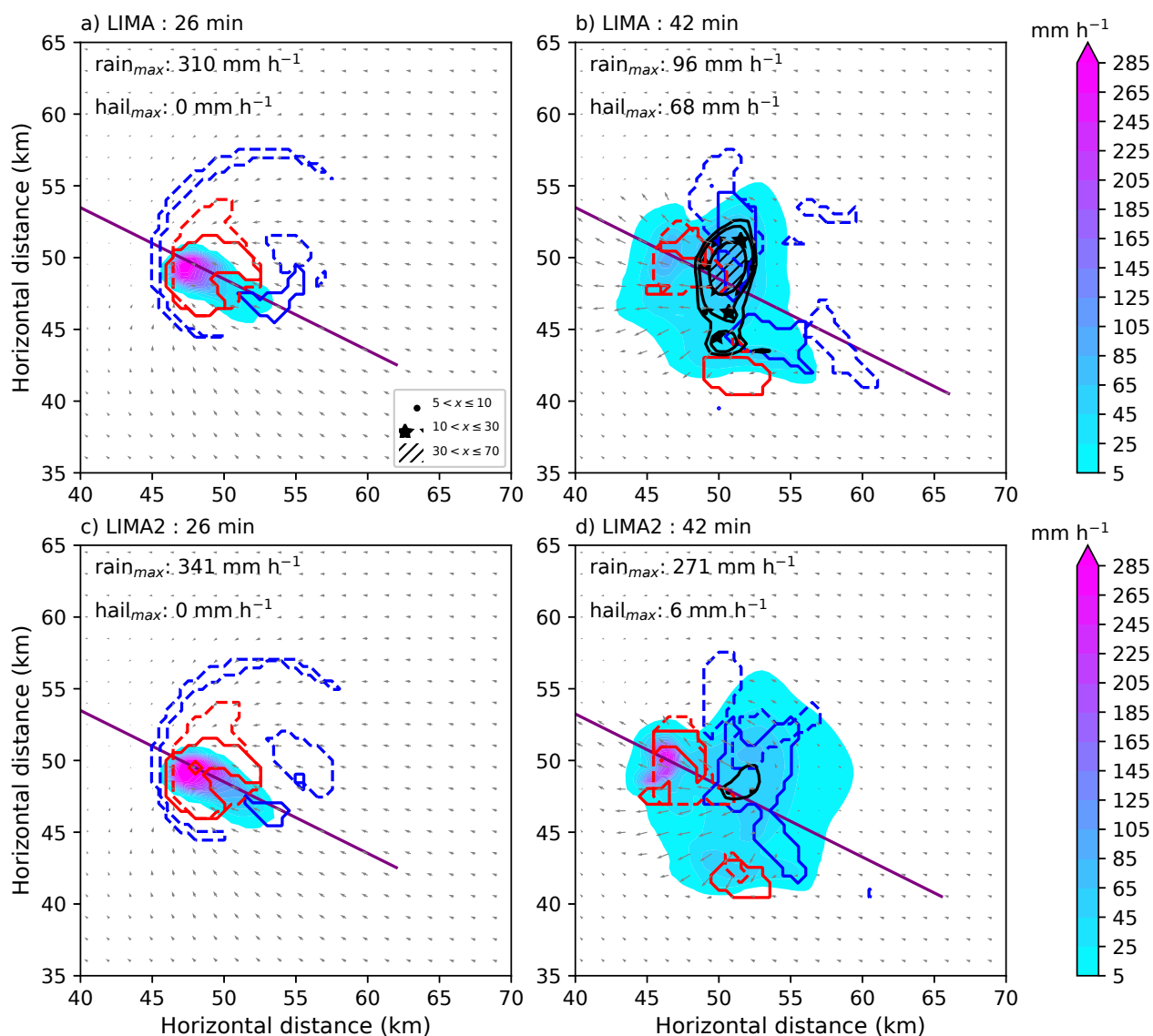


**Figure 4.** Instantaneous rain precipitation (colors) and hail precipitation (lines) at the ground for the LIMA (a-b) and LIMA2 (c-d) simulations at 26 min and 42 min (left and right columns, respectively). The area where the mean vertical wind speed between 0 and 4km (dashed lines) 4 and 8 km (plain lines) exceeds  $5\text{m s}^{-1}$  (red) and  $-1.5\text{m s}^{-1}$  (blue).

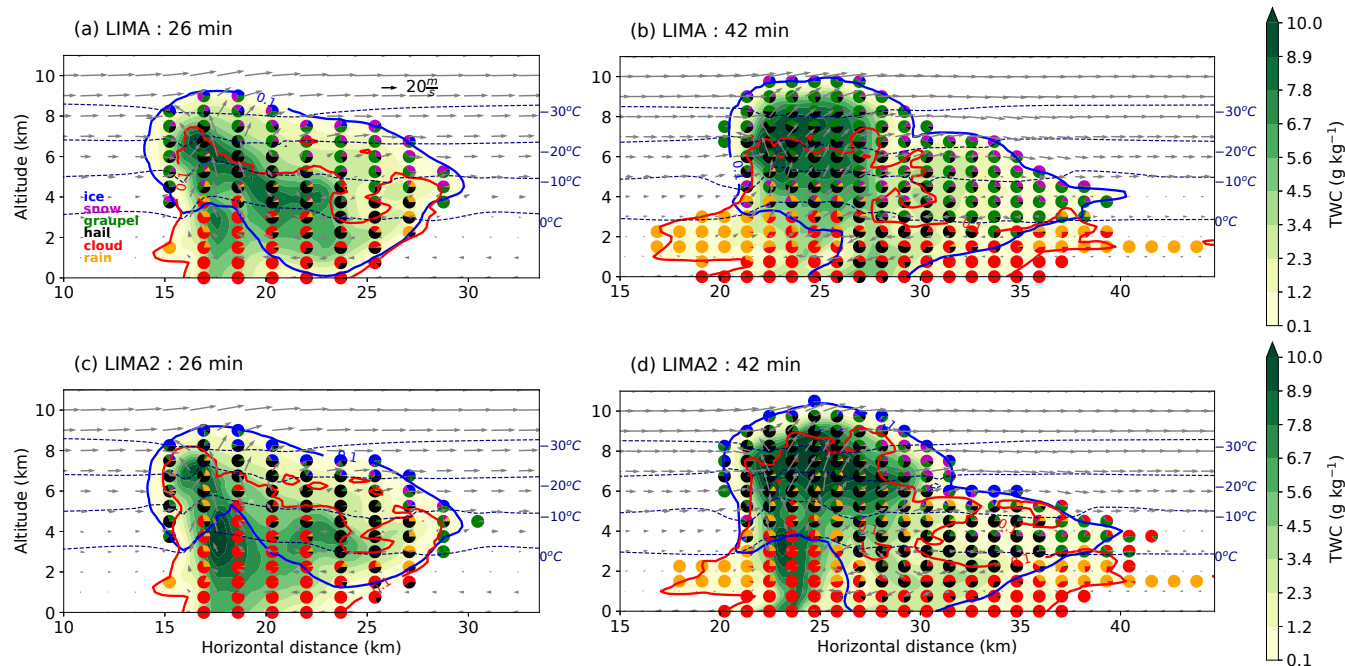


**Figure 5.** Vertical cross sections of the cloud structure passing through the maximum updraft speed and along the zonal axis in LIMA (a-b) and LIMA2 (c-d) simulations after 26 min (left) and after 42 min (right) of simulation. The pie charts show the ratio of each hydrometeor mass in the grid mesh (red for rain, orange for cloud, blue for ice, purple for snow, green for graupel and black for hail). The colors represent the total hydrometeor mass ( $\text{g kg}^{-1}$ ) in each grid mesh. The  $-30^\circ\text{C}$ ,  $-20^\circ\text{C}$ ,  $-10^\circ\text{C}$  and  $0^\circ\text{C}$  (black dashed line) isotherms and the contours of the liquid (red) and solid (blue) water content ( $0.1\text{g kg}^{-1}$ ) are shown. Black arrows represent wind speed and direction, the quiver key is referenced on a).

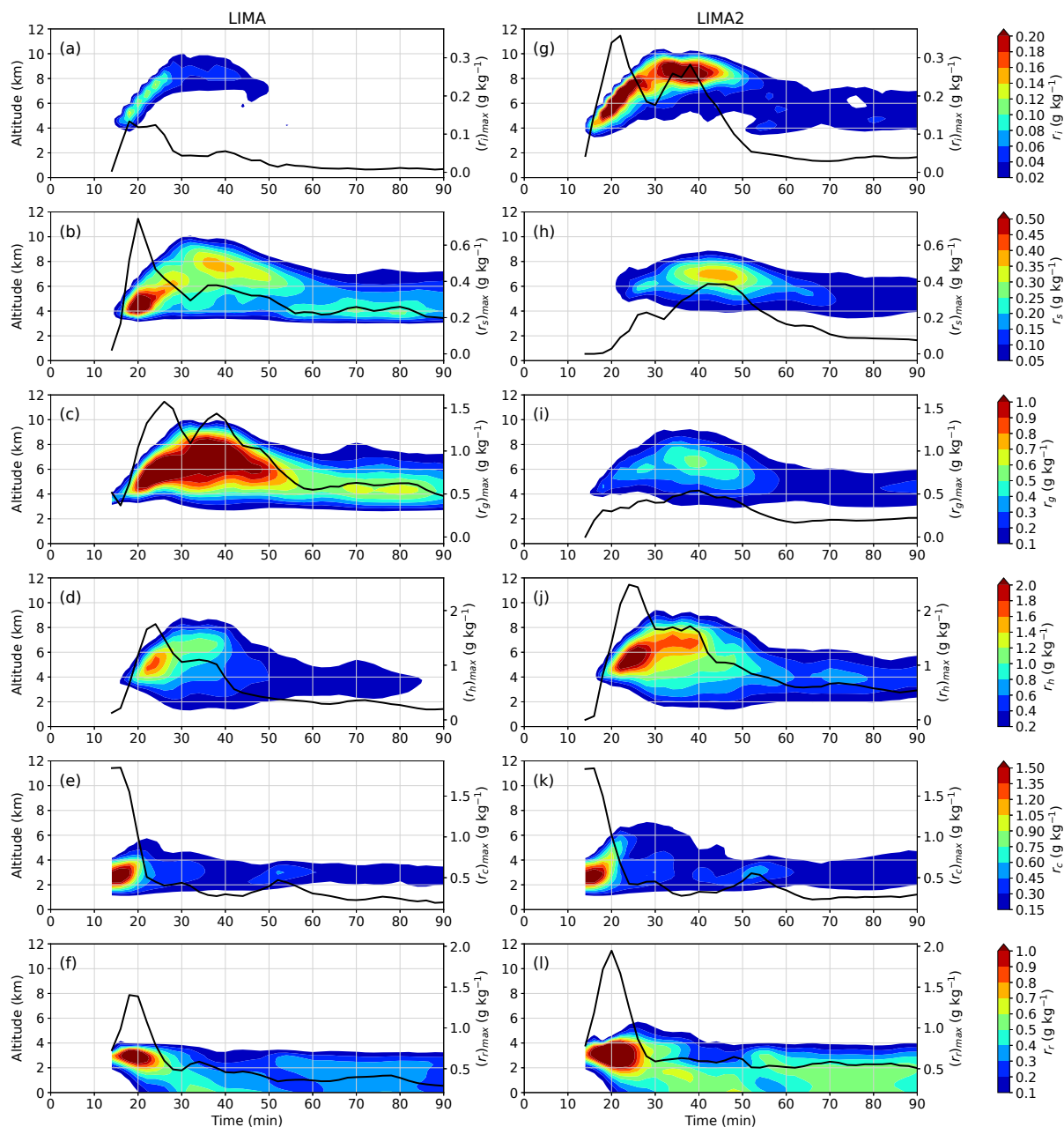


**Figure 6.** Temporal evolution of different hydrometeors vertical mean profiles in LIMA (a-f) and LIMA2 (g-l) simulations. The mean mixing ratio (in  $\text{g kg}^{-1}$ ) is computed using columns where the precipitating hydrometeor is greater than 0.5mm, and is represented, from the top to the bottom, for pristine ice crystals ( $r_i$ ), snow aggregates ( $r_s$ ), graupel ( $r_g$ ), hail ( $r_h$ ), cloud droplets ( $r_c$ ), and raindrops ( $r_r$ ). For each hydrometeor, the time evolution of the maximum mixing ratio is represented by solid lines (right axis).

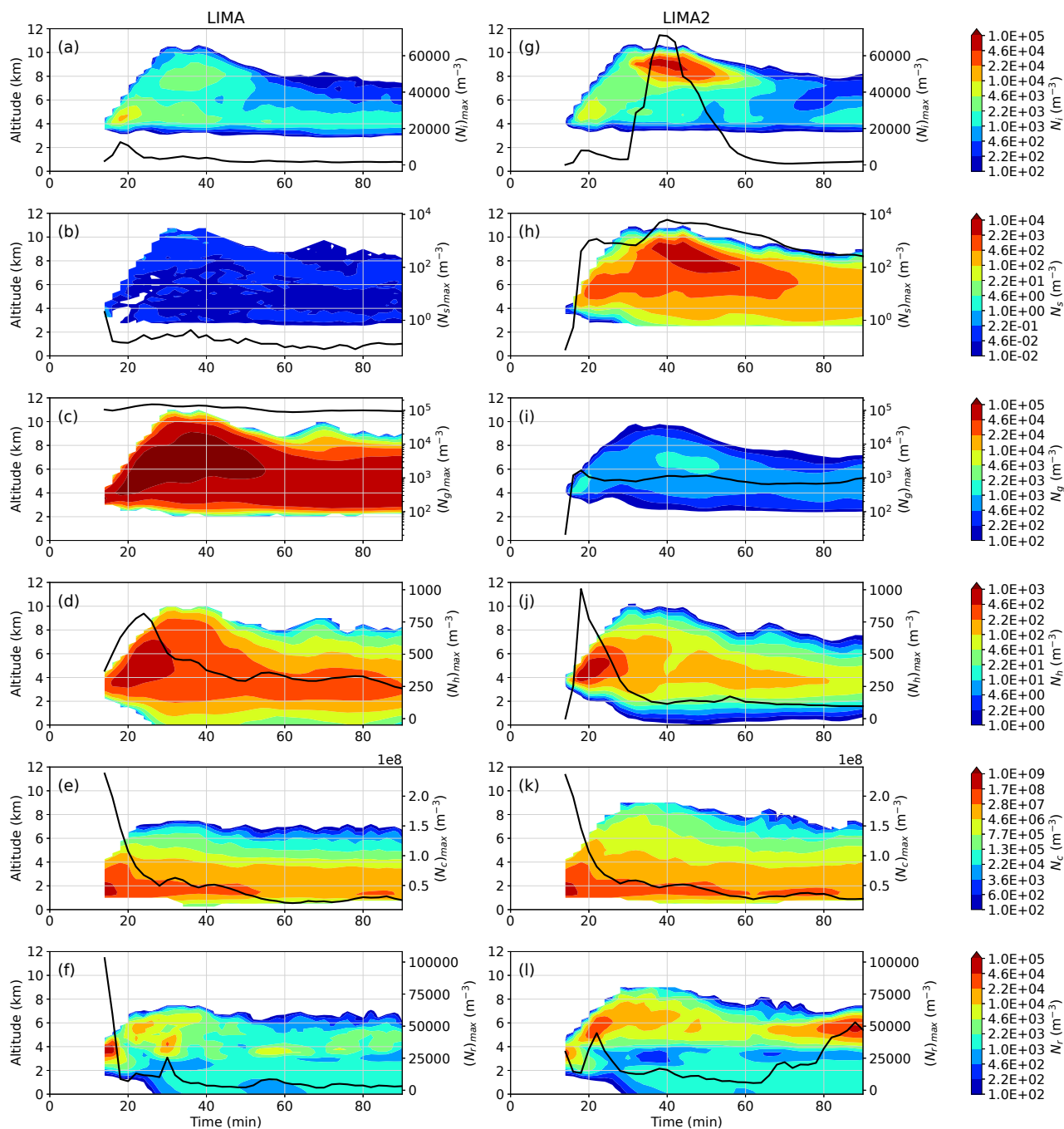
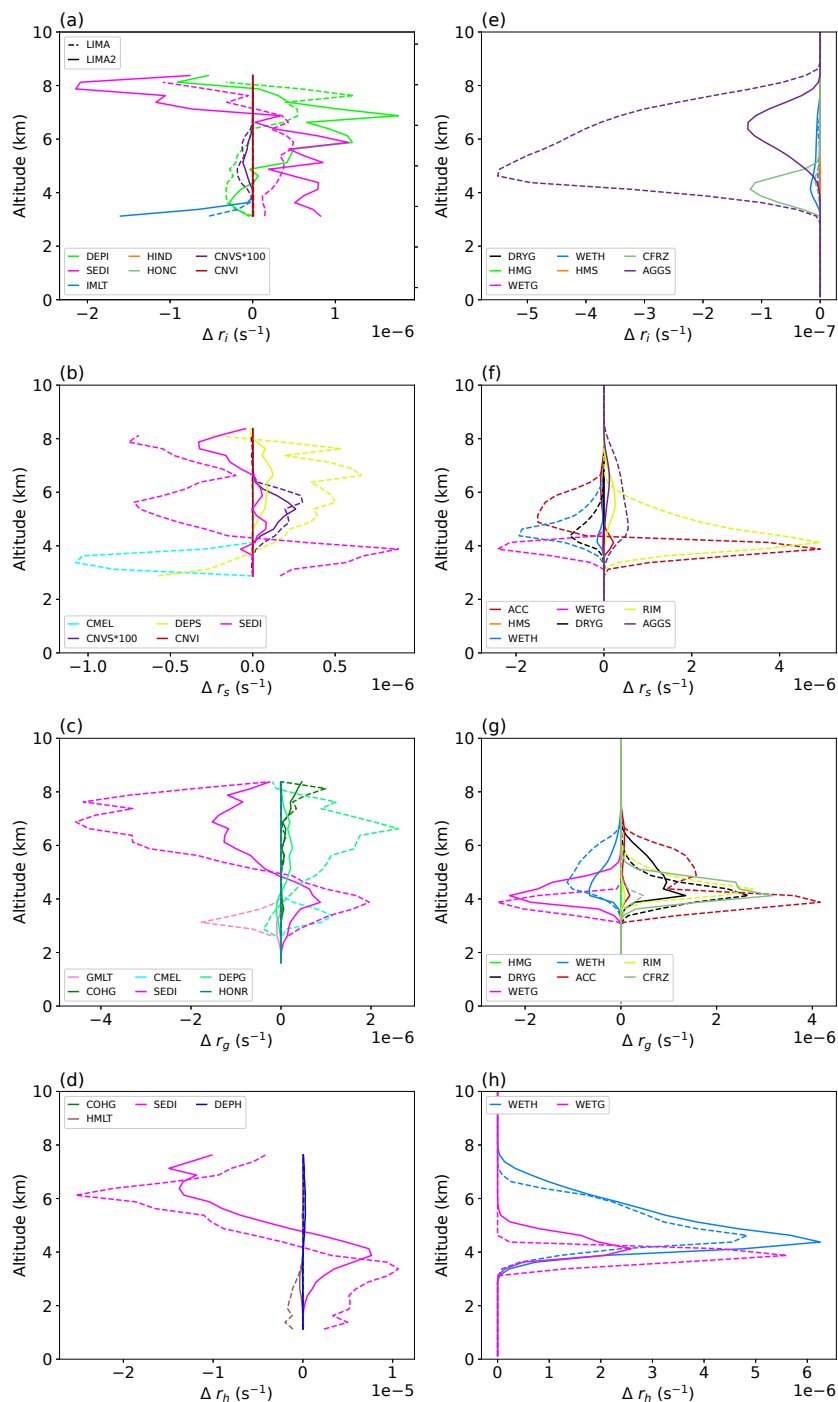
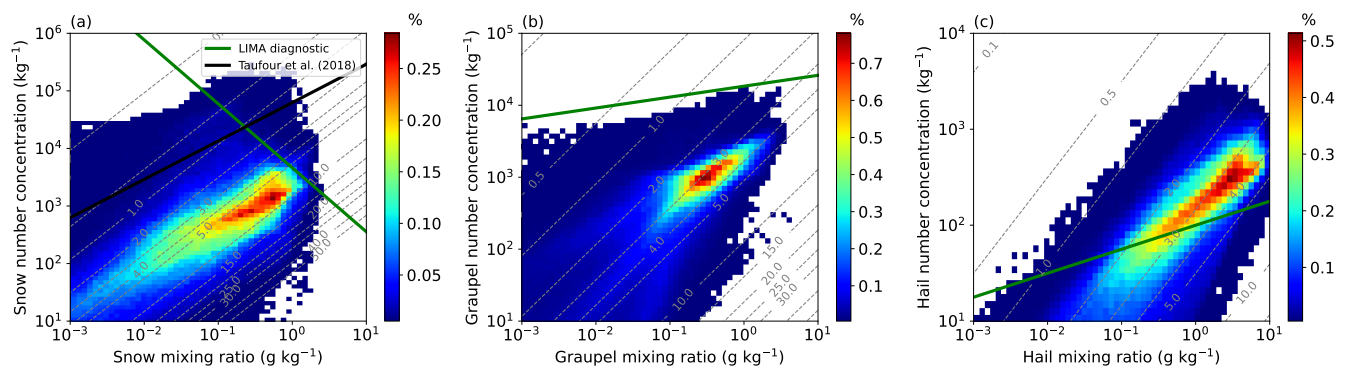


Figure 7. Same as Figure 6 with hydrometeor number concentrations.





**Figure 8.** Weighted averaged vertical profiles for each process transfer rate (colors) for LIMA (dashed lines) and LIMA2 (plain lines) simulations. The profiles are average weighted by the corresponding hydrometeor content used to produce the Figure 6 between 14 and 24 minutes for the processes except collection (a-d) and all the collection processes (e-h)



**Figure 9.** Frequency diagram normalized by the total number of points as a function of mass ( $\text{g kg}^{-1}$ , x-axis) and number ratio ( $\text{kg}^{-1}$ , y-axis) of (a) snow aggregates, (b) graupel, and (c) hail. The green lines show the parameterization used in the LIMA scheme ( $N = C\lambda^x$ ) and the black line on (a) shows the relationship found using airborne in-situ measurements after Taufour et al. (2018). The dashed grey lines represent the mean volume diameter isolines.



**Table 1.** Values of the various parameters used to characterize each water category.

Parameters	ice	snow	graupel	hail	rain	cloud
$\alpha$	3	1	1	1	1	3 on sea; 1 on land
$\nu$	3	1	1	8	1	1 on sea; 3 on land
$a$	0.82	0.02	19.6	470	524	524
$b$	2.5	1.9	2.8	3	3	3
$c$	800	5.1	124	207	842	$3.2 \cdot 10^7$
$d$	1.00	0.27	0.66	0.64	0.8	2
$C$		5	$5 \cdot 10^5$	$4 \cdot 10^4$	$8 \cdot 10^6$	
$x$		1	-0.5	-1	-1	
$\bar{f}_0$	1.00	0.86	0.86	0.86	1.00	
$\bar{f}_1$		0.28	0.28	0.28	0.26	
$\bar{f}_2$	0.14			0		
$\mathcal{C}_1$	$1/\pi$	$1/\pi$	0.5	0.5	0.5	



**Table 2.** List of the LIMA v2.0 microphysical processes.

Process	Symbol	Sink	Source
warm phase processes			
heterogeneous nucleation	HENU	$r_v, N_{CCN, CIN}$	$r_c, N_c$
autoconversion of cloud droplets	AUTO	$r_c, N_c$	$r_r$
accretion of cloud droplets by raindrops	ACC	$r_c, N_c$	$r_r$
self collection of droplets	SC	$N_c$	$\emptyset$
self collection of drops / break-up	SC / BU	$N_r$	$\emptyset$
cloud droplets evaporation(/condensation)	EVAP (/CND)	$r_c, N_c (lr_v)$	$r_v (lr_c)$
rain drops evaporation	EVAP	$r_r, N_r$	$N_c, r_v$
cold phase processes			
heterogeneous nucleation	HEN	$r_v, N_{IFN, CIN}$	$r_i, N_i$
autoconversion of pristine ice	CNVI	$r_i, N_i$	$r_s, N_s$
sublimation of aggregates	CNVS	$r_s, N_s$	$r_i, N_i$
aggregation of pristine ice	AGG	$r_i, N_i$	$r_s$
self collection of snow/aggregates	SC	$N_s$	$\emptyset$
dry growth of the graupels	DRYG	$r_i, r_s, N_i, N_s$	$r_g$
wet growth of the graupels	WETG	$r_i, r_s, N_i, N_s$	$r_g$
conversion melting	CMEL	$r_s, N_s$	$r_g, N_g$
deposition on ice crystals (/sublimation)	DEPI (/SUB)	$r_v (lr_i, N_i)$	$r_i (lr_v)$
deposition on snow/aggregates (/sublimation)	DEPS (/SUB)	$r_v (lr_s, N_s)$	$r_s (lr_v)$
deposition on graupel (/sublimation)	DEPG (/SUB)	$r_v (lr_g, N_h)$	$r_g (lr_v)$
deposition on hail (/sublimation)	DEPH (/SUB)	$r_v (lr_h, N_h)$	$r_h (lr_v)$
mixed phase processes			
homogeneous nucleation	HONR	$r_r, N_r$	$r_g, N_g$
immersion freezing of coated IFN	IFR	$r_c, N_c$	$r_i, N_i$
raindrops contact freezing	CFRZ	$r_r, r_i, N_r, N_i$	$r_g, N_g$
light riming of aggregates	LRIM	$r_c, N_c$	$r_s$
heavy riming of aggregates	HRIM	$r_c, r_s, N_c, N_s$	$r_g, N_g$
accretion of rain and aggregates	ACC	$r_r, r_s, N_r, N_s$	$r_s, r_g, N_g$
Hallet-Mossop process	HMS-G	$r_s, r_g$	$r_i, N_i$
Homogeneous nucleation	HONC	$r_c (/N_c)$	$r_i, N_i$
dry growth of the graupels	DRYG	$r_c, r_r, N_r, N_c$	$r_g$
partial freezing & water shedding	WETG & SHED	$r_c, r_r, N_r, N_c$	$r_g, N_r$
ice melting	IMLT	$r_i, N_i$	$r_c, N_c$
graupel melting	GMLT	$r_g, N_g$	$r_r, N_r$
hail melting	HMLT	$r_h, N_h$	$r_r, N_r$